

# Rapid, Ultrasensitive, and Quantitative Detection of SARS-CoV-2 Using Antisense Oligonucleotides Directed Electrochemical Biosensor Chip

Maha Alafeef,<sup>#</sup> Ketan Dighe,<sup>#</sup> Parikshit Moitra,<sup>#</sup> and Dipanjan Pan\*



Cite This: <https://dx.doi.org/10.1021/acsnano.0c06392>



Read Online

ACCESS |



Metrics & More



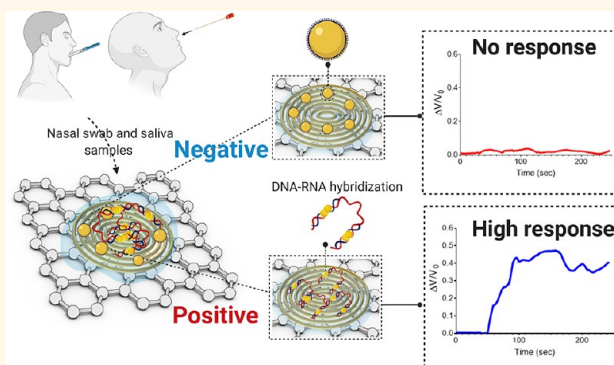
Article Recommendations



Supporting Information

**ABSTRACT:** A large-scale diagnosis of the severe acute respiratory syndrome-coronavirus-2 (SARS-CoV-2) is essential to downregulate its spread within as well as across communities and mitigate the current outbreak of the pandemic novel coronavirus disease 2019 (COVID-19). Herein, we report the development of a rapid (less than 5 min), low-cost, easy-to-implement, and quantitative paper-based electrochemical sensor chip to enable the digital detection of SARS-CoV-2 genetic material. The biosensor uses gold nanoparticles (AuNPs), capped with highly specific antisense oligonucleotides (ssDNA) targeting viral nucleocapsid phosphoprotein (N-gene). The sensing probes are immobilized on a paper-based electrochemical platform to yield a nucleic-acid-testing device with a readout that can be recorded with a simple hand-held reader. The biosensor chip has been tested using samples collected from Vero cells infected with SARS-CoV-2 virus and clinical samples. The sensor provides a significant improvement in output signal only in the presence of its target—SARS-CoV-2 RNA—within less than 5 min of incubation time, with a sensitivity of  $231 \text{ (copies } \mu\text{L}^{-1})^{-1}$  and limit of detection of 6.9 copies/ $\mu\text{L}$  without the need for any further amplification. The sensor chip performance has been tested using clinical samples from 22 COVID-19 positive patients and 26 healthy asymptomatic subjects confirmed using the FDA-approved RT-PCR COVID-19 diagnostic kit. The sensor successfully distinguishes the positive COVID-19 samples from the negative ones with almost 100% accuracy, sensitivity, and specificity and exhibits an insignificant change in output signal for the samples lacking a SARS-CoV-2 viral target segment (e.g., SARS-CoV, MERS-CoV, or negative COVID-19 samples collected from healthy subjects). The feasibility of the sensor even during the genomic mutation of the virus is also ensured from the design of the ssDNA-conjugated AuNPs that simultaneously target two separate regions of the same SARS-CoV-2 N-gene.

**KEYWORDS:** COVID-19, SARS-CoV-2, electrochemical sensor, gold nanoparticles, antisense oligonucleotide



The emergence of novel viruses has often ravaged humanity and thus marked its devastating footprint in the course of modern history. Viruses such as yellow fever, influenza H1N1, polio, human immune deficiency virus (HIV), severe acute respiratory syndrome (SARS), Middle East respiratory syndrome (MERS) coronaviruses, Ebola, and Zika virus have led to pandemics, affecting health and the global economy.<sup>1</sup> Despite the ever-persistent threat of an emerging disease outbreak, a widespread public health initiative to prepare for never-before-seen illnesses remains minimal. A lack of a rapid, affordable, and reliable molecular diagnostic test has impacted the global response to new viral threats.<sup>2–4</sup> Therefore, improvements in health care, availability

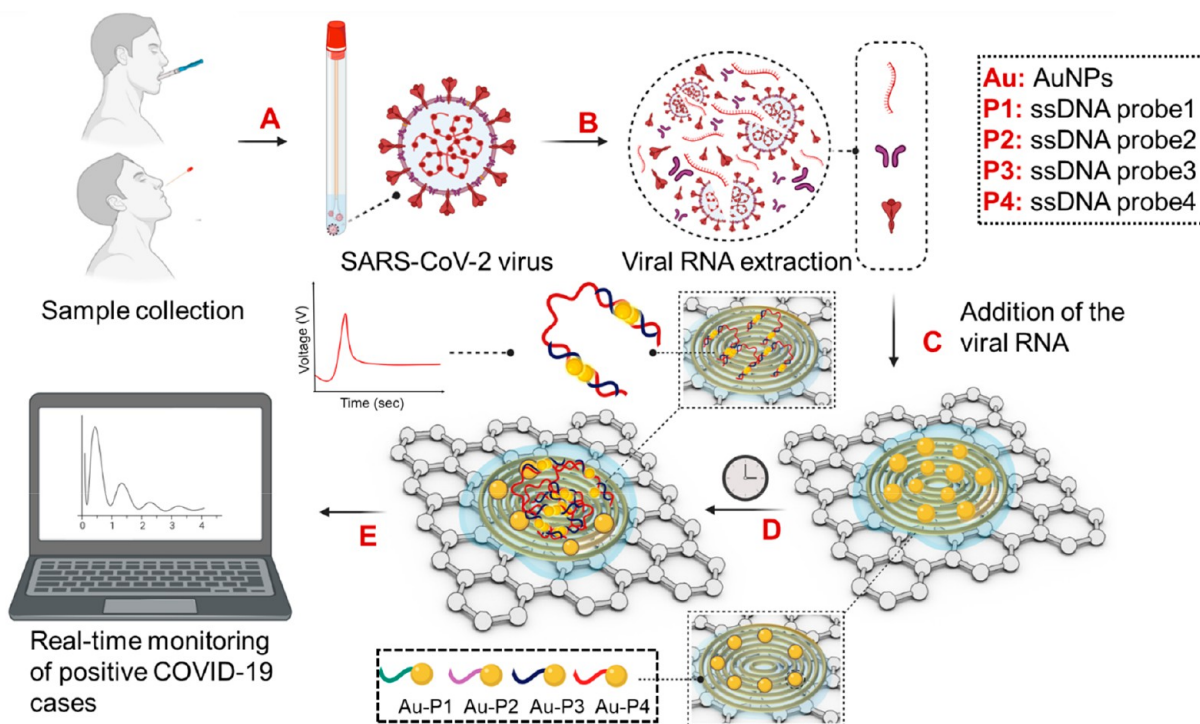
of rapid and accurate testing, and understanding the factors that incubate pandemics could be powerful tools to mitigate its impact. In this regard, the latest threat to global health is the outbreak of novel coronavirus disease 2019 (COVID-19), caused by a severe acute respiratory syndrome-coronavirus-2

Received: July 30, 2020

Accepted: October 13, 2020



**Scheme 1.** Schematic representation of the operation principle of the COVID-19 electrochemical sensing platform wherein step A: the infected samples will be collected from the nasal swab or saliva of the patients under observation; step B: the viral SARS-CoV-2 RNA will be extracted; step C: the viral RNA will be added on top of the graphene-ssDNA-AuNP platform; step D: incubation of 5 min; and step E: the digital electrochemical output will be recorded.



(SARS-CoV-2).<sup>5</sup> This outbreak was first recognized in December 2019 and has since rapidly spread across the globe, affecting the socioeconomic conditions of billions of people worldwide.<sup>6,7</sup> It has been reported that COVID-19 cases present a variety of clinical symptoms ranging from moderate flu-like to life-threatening complications.<sup>8,9</sup> Besides, the asymptomatic transmission of SARS-CoV-2 is the Achilles' heel of the currently deployed public health strategies to mitigate this pandemic.<sup>10</sup> Therefore, the ability to perform widespread, accurate, and rapid testing is extremely crucial in understanding the complex dynamics involving SARS-CoV-2 infection and immunity.<sup>11</sup> Toward this end, scientists across the globe have been vying for the development and production of rapid and accurate diagnostic tests.

Currently, the diagnostic tests for COVID-19 can be classified into two broad categories. The first category includes the molecular diagnostic test for the identification of SARS-CoV-2 viral RNA using reverse transcriptase real-time polymerase chain reaction (RT-PCR) and nucleic acid hybridization strategies.<sup>12,13</sup> Although RT-PCR is excellent in terms of selectivity and sensitivity, it is time-intensive, requires highly qualified personnel, and can only be operated in a laboratory-based hospital with the accessibility of large stationary equipment and reagents.<sup>14,15</sup> These restrictions become major footcages for situations with resource shortages. The second category includes serological and immunological tests that primarily focus on the detection of antibodies developed in individuals because of their exposure to the virus.<sup>16,17</sup> While these tests are rapid and require minimal equipment, their clinical utility to indicate COVID-19 infection is limited, as it may take several days to weeks after the onset of the symptoms for a patient to develop a detectable

antibody response.<sup>18–20</sup> Hence, a highly sensitive diagnostic method with rapid and continuous monitoring of SARS-CoV-2 is required to obtain valued information that could support physicians in better treatment of COVID-19-related conditions.

In recent years there have been several reports of point-of-care (POC) biosensor development using 2D nanomaterials for ultrasensitive diagnosis of different diseases.<sup>21–23</sup> Among these 2D nanomaterials, mainly graphene has come to be the most compelling nanomaterial due to its intrinsic properties.<sup>24–26</sup> Moreover, electrochemical techniques are considered as a cost-effective approach due to its simplicity of service, high sensitivity, rapid response, miniaturization, and ease of use in molecular diagnostics.<sup>27</sup> To date, numerous graphene-based electrochemical biosensors have been reported to detect a wide range of chemical and biological targets such as small molecules, metal ions, proteins, bacteria, and nucleic acids.<sup>28–33</sup> Various electrochemical immunosensors for influenza virus have been documented using differential pulse voltammetry (DPV),<sup>34</sup> impedance spectroscopy (EIS),<sup>35</sup> linear sweep voltammetry,<sup>36,37</sup> chronoamperometry,<sup>38</sup> and cyclic voltammetry.<sup>39</sup> Additionally, an electrochemical immunosensor with good selectivity and enhanced detection limit has also been documented for label-free influenza virus detection.<sup>40</sup> HIV was identified using DPV on a multiwalled carbon nanotube modified glass carbon electrode (GCE),<sup>41</sup> whereas human papillomavirus (HPV) was determined using a graphene/Au nanorod/polythionine-modified GCE via DPV and EIS.<sup>42</sup>

Herein, we have developed a graphene-based electrochemical biosensor coupled with an electrical readout setup to selectively detect the presence of SARS-CoV-2 genetic

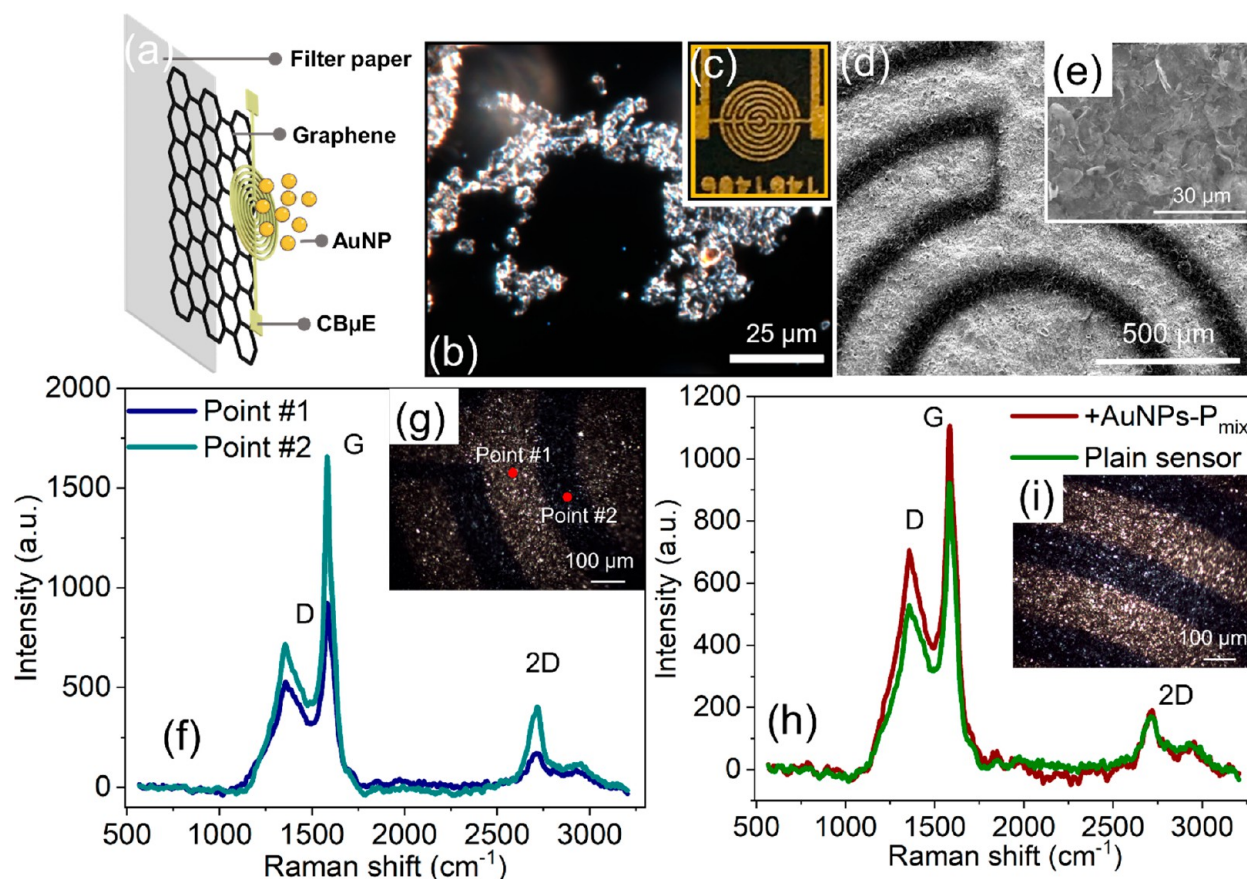


**Figure 1.** (a) Zoom-in image illustrating the layer-by-layer construct of the sensor. (b) Dark-field image of the graphene film. (c) Photograph of the graphene sensor platform. (d, e) SEM images of the graphene-based platform. (f) Raman spectrum of the plain sensor chip of two spatial points, point 1: a spot located on the gold electrodes, point 2: a spot located on the graphene coating of the filter paper. (g) The microscope image of the plain sensor used to record the Raman spectrum in (f). (h) Comparison of the Raman spectrum of the sensor chip before and after the deposition of ssDNA-capped gold nanoparticles. (i) Microscope image of the sensor used to record the Raman spectrum in (h).

material. The selectivity of the biosensor originates from the integration of a suitable design of thiol-modified antisense oligonucleotides (ssDNA) specific for nucleocapsid phosphoprotein (N-gene) of SARS-CoV-2. Four such ssDNA probes were designed to target two separate regions within the same viral N-gene at the same time,<sup>43</sup> which also increased the analytical performance of the assay when compared with the electrochemistry of individual ssDNA. The sensitivity of the electrochemical assay was further improved by the application of thiol-modified ssDNA-capped gold nanoparticles (AuNPs) on top of the gold electrode in contrast to the ssDNA alone with no AuNP conjugation. The sensor response has been validated against the RNA samples obtained from Vero cells infected with SARS-CoV-2, while SARS-CoV and MERS-CoV RNA has been used as one of the negative controls. The capability of the sensor chip to differentiate the positive COVID-19 samples from the negative ones has been investigated using 48 clinical samples, and the results were benchmarked using an FDA-approved gold-standard SARS-CoV-2 diagnostic method (LabGun COVID-19 RT-PCR diagnostic kit). Our results indicated that the specific output signal from SARS-CoV-2 could be obtained within less than 5 min of incubation of the RNA samples with a sensitivity of 231 ((copies  $\mu\text{L}^{-1}$ )<sup>-1</sup>)<sup>-1</sup> and limit of detection of 6.9 copies/ $\mu\text{L}$ . Using clinical samples collected from 22 COVID-19 positive patients and 26 healthy asymptomatic subjects—confirmed

using the RT-PCR test—the sensor was successful in distinguishing the positive COVID-19 samples from the negative ones with high accuracy, sensitivity, and specificity. Overall, we report herein a methodology for rapid, accurate, selective, and ultrasensitive detection of COVID-19 causative virus, SARS-CoV-2, by precise digital monitoring of the electrochemical response generated from the graphene-ssDNA-AuNP surface (Scheme 1).

## RESULTS AND DISCUSSION

**Fabrication and Characterization of the Paper-Based Electrochemical Platform.** The central theme of this study is schematically shown in Figure 1a, which depicts a graphene-based electrochemical platform for selective and ultrasensitive detection of SARS-CoV-2 viral RNA by exploiting high specific ssDNA-capped gold nanoparticles as the sensing element. Although the graphene-based electrochemical platform has been quite explored in the past decade, the design of an electrochemical sensor based on the antisense oligonucleotides targeted specifically toward the rapid, selective, ultrasensitive detection of SARS-CoV-2 viral RNA has not yet been explored. Further, introducing the ssDNA-capped gold nanoparticles to the electrochemical sensing platform made the current technology quite eligible to sense the viral RNA without any gene amplification step with a reasonably lower detection limit compared with other conventional methods.



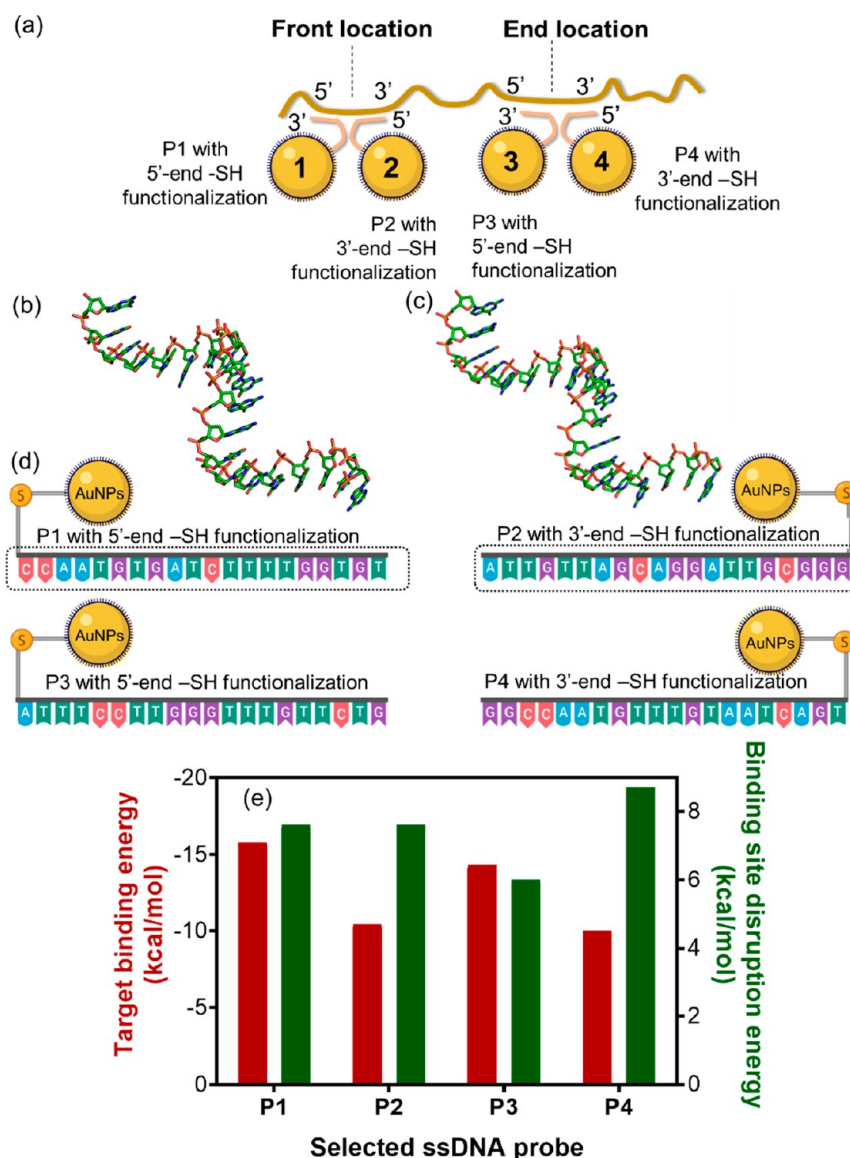


**Figure 2.** (a) Design principle of antisense oligonucleotides with differential functionalized ends. The yellow dot in the figure represents the ssDNA-conjugated gold nanoparticles. Backbone 3D structure of (b) antisense ssDNA probe 1 (P1) and (c) antisense ssDNA probe 2 (P2). (d) Differentially functionalized AuNPs with thiol-ended ssDNA probes along with their sequences. (e) Comparative target N-gene binding and binding site disruption energies of the four selected ssDNA probes.

The current pandemic situation demands the need for the development of a low-cost POC sensor that can diagnose positive COVID-19 cases with high accuracy, sensitivity, and specificity without the need for specialized chemicals, complex fabrication procedures, and sophisticated equipment. In this regard, we employed simple two-step procedures to develop a paper-based electrical sensor chip that can diagnose positive COVID-19 cases within a few minutes without the need for further gene amplification procedures. A graphene suspension was first coated on filter paper to form a conductive film followed by the deposition of a Au electrode with a predefined design. A schematic of this biosensor construct is shown in Figure 1a. Graphene nanoplatelets (GR) provide the advantage of preventing the formation of a water-tight composite on the sensor chip, thereby giving an edge-over-edge configuration of the film at the microscopic level.<sup>31</sup> The high carrier mobility ( $>2000 \text{ cm}^2 \text{ V s}^{-1}$ ) of graphene also makes it highly sensitive to the interaction and adsorption of the charged target at its

surface. Figure 1b depicts the dark-field image of the graphene film with the AuNPs in the absence of SARS-CoV-2 RNA. The photograph of the developed chip is shown in Figure 1c. Figure 1d,e show the scanning electron microscopic (SEM) image of the sensor chip, which shows both the edge-over-edge microscopic configuration of the graphene nanoplatelets and the pattern of gold electrodes. The electrochemical sensor thus utilizes a paper base coated with a thin graphene conductive film and carefully designed gold electrode. The graphene film plays an important role in the sensing response. To optimize the graphene film, the concentration of the graphene suspension used for making the graphene film has been varied and the resistance of the graphene film on the filter paper was measured directly. Three different concentrations of graphene platelets (*i.e.*, 5, 10, and 20 mg/mL) have been used to make three graphene films using the same procedure as described in the Experimental Section. A thick and viscous suspension was formed while utilizing a graphene concentration of 20 mg/mL,

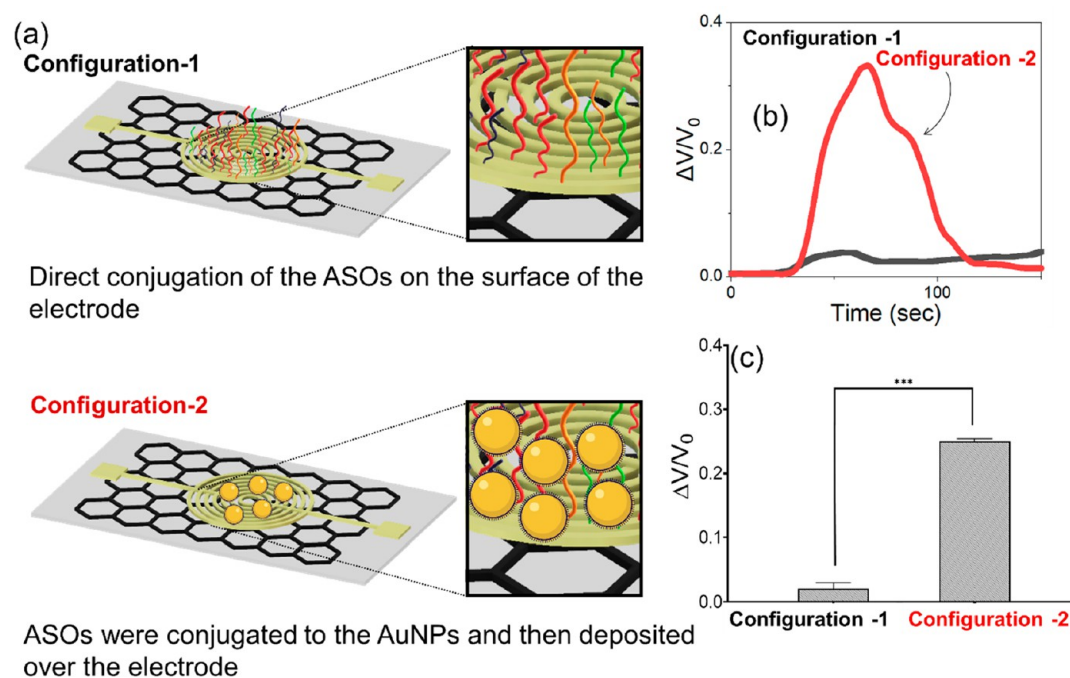


**Figure 3.** (a) Schematic representation of the proposed concept behind the enhancement in electrochemical response using gold nanoparticles, when capped with ssDNA probes. (b) Relative change in the biosensor output voltage for the two sensor configurations. (c) Comparative biosensor signal output for both sensor configurations.

which makes it difficult to form a uniformly coated surface. On the other hand, the texture of the suspension having a concentration of 10 or 5 mg/mL was reasonable to uniformly coat the filter paper surface. Figure S1 illustrates the  $V-I$  response of the graphene film made from two different graphene concentrations. The 5 mg/mL film showed a nonlinear  $V-I$  response ( $R^2 = 0.28$ )—not obeying Ohm's law—and very low response when compared to the film made from the 10 mg/mL suspension. Moreover, the 10 mg/mL film shows a linear  $V-I$  response ( $R^2 = 0.99$ ) and with a base resistance of 272.4 ohms. Therefore, the graphene film from a 10 mg/mL suspension has been used to make the sensor chip, which was used throughout this work.

Recently, nanoparticles have shown their promise in improving the sensing and recognition performance of SARS-CoV-2.<sup>43–48</sup> Accordingly, we used gold nanoparticles to increase the sensitivity of our electrochemical platform due to their excellent unmatched properties.<sup>49–51</sup> Citrate-stabilized AuNPs of  $10 \pm 5$  nm in size were synthesized using a previous literature report<sup>52</sup> and used in the electrochemical sensor chip. Transmission electron microscopy images of the as-synthesized gold nanoparticles revealed the anhydrate particle diameter (Figure S2). The hydrodynamic diameter of the citrate-stabilized nanoparticles was found to be  $44.7 \pm 5.9$  nm, and the zeta potential measurement revealed the colloidal stability of these particles with  $\zeta = -50.24 \pm 6.07$  mV. To achieve selectivity and sensitivity during the recognition of SARS-CoV-2 genetic material, we used ssDNA—known as probes throughout the article—capped AuNPs, which were then deposited on the surface of the sensor platform. Raman spectra have been collected to further characterize the sensor chip. The plain sensor shows a high  $I_G/I_D$  ratio in the presence of the gold electrode compared to the absence of it, with a higher 2D peak in the graphene region (Figure 1f,g), confirming the successful mounting of the gold electrodes on top of the

graphene film. Further, it can be seen from the Raman spectral analysis that the graphene base provides a graphitic ( $sp^2$ ) to diamond ( $sp^3$ ) intensity ratio ( $I_G/I_D$ ) of 1.74, while the sensor immobilized with the ssDNA-capped gold nanoparticle has an  $I_G/I_D$  value of 1.56 (Figure 1e,h). This decrease in  $I_G/I_D$  value can be attributed to the surface-enhanced Raman scattering (SERS) caused by the presence of the AuNPs on gold electrodes. Furthermore, the graphitic wavenumber is also downshifted from 1584 to 1581  $cm^{-1}$ , which indicates the increased  $\pi-\pi$  interactions between the oligonucleotide (ssDNA) and graphene.<sup>17,53,54</sup> Once the viral sample encounters the sensor, viral RNA hybridizes with the AuNP-capped ssDNA, allowing a more accurate electrochemical measurement. The ssDNA probes have been designed based on a previous report from our research group<sup>43</sup> and are described in the following section.

**Strategic Design of the Antisense Oligonucleotide, ssDNA, Probes for Targeting SARS-CoV-2 Viral RNA.** Three regions among the SARS-CoV-2-related viral genomes have been identified as the conserved sequences among which an assay targeting the N-gene (nucleocapsid phosphoprotein) has recently been recommended as a screening test to determine positive COVID-19 cases.<sup>12</sup> Scientists are therefore continually trying to ease the screening protocol for the N-gene due to the current upsurge of test kits' requirement to selectively identify and quarantine SARS-CoV-2-infected personnel.<sup>12,55</sup> We, therefore, thought of a simple paper-based gold nanoparticle-mediated electrochemical assay to easily and quickly detect the presence of the SARS-CoV-2 N-gene from an infected RNA sample. The methodology described herein utilizes a multimodal approach that simultaneously targets two separate regions of the N-gene at the same time using four different suitably functionalized gold nanoparticles (Figure 2a–c). These AuNPs were individually capped with four of the carefully designed antisense

oligonucleotides (ssDNA probes). Nevertheless, this strategy is supposed to increase the reliability and feasibility of the electrochemical assay even if there is a mutation in the viral gene during its cross-transmission because of its multimodal approach of targeting the viral genome. This electrochemical assay is therefore believed to enhance the analytical sensitivity of the N-gene.

In order to design ssDNA probes selective for SARS-CoV-2, the genome sequence of SARS-CoV-2 isolate 2019-nCoV/USA-WA1-A12/2020 was considered and its N-gene was undertaken for the prediction of a set of antisense oligonucleotide probes as described in the [Materials and Methods](#) section. The target binding energies and binding disruption energies of the predicted probes were compared, and the ones with the optimum energies have been selected ([Figure 2e](#) and [Table S1](#)). One other criterion behind the selection of these four probes is their relatively close target positions. The antisense probe, P1, targets the N-gene sequence 421–440, whereas P2 targets the sequence 443–462. On the other hand, P3 targets the sequence position 836–855, whereas antisense P4 targets the 886–905 position of the N-gene. The ssDNA probes were then functionalized differentially: 5' ends of P1 and P3 were modified and 3' ends of P2 and P4 were altered with thiol moieties having a six-carbon spacer ([Figure 2d](#)). These ssDNA probes were then used to cap gold nanoparticles and loaded over the gold electrode to accelerate the electron transfer followed by enhancement in the electrochemical response of graphene toward the selective detection of SARS-CoV-2. The successful surface capping of AuNPs with ssDNA probes was confirmed from their relative change in the UV–vis absorbance spectrum ([Figure S3](#)), the change of the electrophoretic mobility in agarose gel electrophoresis ([Figure S4](#)). Citrate-capped AuNPs without any DNA barely migrated, whereas the ssDNA-capped AuNPs migrated differentially plausibly due to their differential surface functionalization with ssDNA probes. The differential electrophoretic mobility of the gold nanoparticles indicated the differential surface charge associated with the nanoparticles.<sup>56,57</sup> It can therefore be inferred that more ssDNA functionalization will lead to a more surface negative charge and hence more electrophoretic mobility. Thus, it can be said that the ssDNA functionalization is more for Au-P3<sub>H</sub>, followed by Au-P4<sub>M</sub>, Au-P1<sub>M</sub>, and Au-P2<sub>L</sub>.

**Signal Amplification Using Gold Nanoparticles Capped with ssDNA Probes and the Optimization of Probes/AuNPs Ratio and AuNP Size.** The designed antisense oligonucleotides can be incorporated on the sensor chip in two different configurations, as shown in [Figure 3a](#). The antisense probes can be conjugated directly to the gold electrode surface (configuration 1) or can be utilized to cap the surface of gold nanoparticles, which will then be deposited at the surface of the sensor platform (configuration 2). [Figure 3b](#) shows the sensors response after the addition of  $5.854 \times 10^7$  of SARS-CoV-2 viral RNA. Configuration 1—antisense oligonucleotides were thiolated on the gold electrode—provides a low response signal compared to the configuration 2. The sensor response to the SARS-CoV-2 RNA in configuration 2 was found to be significantly higher ( $p < 0.001$ ) compared to the response in configuration 1 ([Figure 3c](#)). This significant increase in electrical signal in the presence of AuNPs—configuration 2—may also be attributed to the increased reactivity of the ssDNA probes when capped on AuNPs and deposited over the electrode surface, favoring the electron

transfer kinetics and also because the AuNPs provided a high surface area for the interaction of ssDNA probes with the viral RNA, eventually leading to signal amplification. On the other hand, the lower electrical responses observed for configuration 1 indicated decreased conductive pathways for electron transfer. Further, AuNPs, due to their excellent conductive characteristics,<sup>58–62</sup> contribute to these conduction pathways by accelerating the electron transfer, leading to the increased output signal in the presence of SARS-CoV-2 viral RNA. Therefore, the sensor with configuration 2, consisting of antisense oligonucleotide-capped AuNPs deposited over the gold electrode, has been used for all our future electrochemical studies.

The sensitivity of the sensor is highly dependent on the recognition element (*i.e.*, antisense oligonucleotide). The density of the ssDNA probe immobilized on the sensor surface is an essential factor affecting the sensitivity and is anticipated to play a role in the sensor response.<sup>63</sup> The developed platform can thus be represented by a resistive sensor model in which the change in the voltage across the sensor chip is given by

$$\Delta V = R \frac{dq}{dt} \quad (1)$$

where  $\Delta V$  is the change in the voltage across the sensor chip,  $R$  is the resistance, and  $q$  is the charge.

We have used the Langmuir model to fit the kinetics of binding as in the surface plasmon resonance (SPR) experiments in which this model has been widely explored at high flow speeds.<sup>64,65</sup> The dissociation to the formation of the binding complex RNA–DNA with an immobilized ssDNA probe (D) at the end of the injection can be given by

$$\frac{d[RD]_t}{dt} = k_d[RD]_t \quad (2)$$

where  $[RD]_t$  is the surface density of the binding complex between the viral RNA and antisense ssDNA,  $[R]$  is the concentration of the target RNA, and  $k_d$  is the dissociation rate constant.

[Equation 2](#) is a first-order equation that can be solved analytically to provide [eq 3](#):

$$[RD]_t = \frac{k_a[D]_{\max}[R]}{k_a[R] + k_d} e^{-k_d t} \quad (3)$$

where  $k_a$  is the association rate constant and  $[D]_{\max}$  is the maximum number of ssDNA probes available for binding per surface area.

The change in the surface charges ( $\Delta q$ ) can be represented by  $Q_{\text{RNA}}S[RD]_t$ <sup>66</sup> where  $Q_{\text{RNA}}$  is the electric charge caused by the adsorbed RNA unit to the sensor chip per surface density, and  $S$  is the graphene surface area. Then, [eq 1](#) can be written as

$$\Delta V = R \frac{dq}{dt} = Q_{\text{RNA}} S \frac{d[RD]_t}{dt} \quad (4)$$

$$\Delta V = R Q_{\text{RNA}} S k_d \frac{k_a[D]_{\max}[R]}{k_a[R] + k_d} e^{-k_d t} \quad (5)$$

Thus, from [eq 5](#), it may be presumed that maximum response will be obtained from an immobilized density of the maximum number of ssDNA probes,  $[D]_{\max}$ . Based on [eq 5](#), a higher response level is thus anticipated when more antisense ssDNA probes are immobilized on the surface. However, the



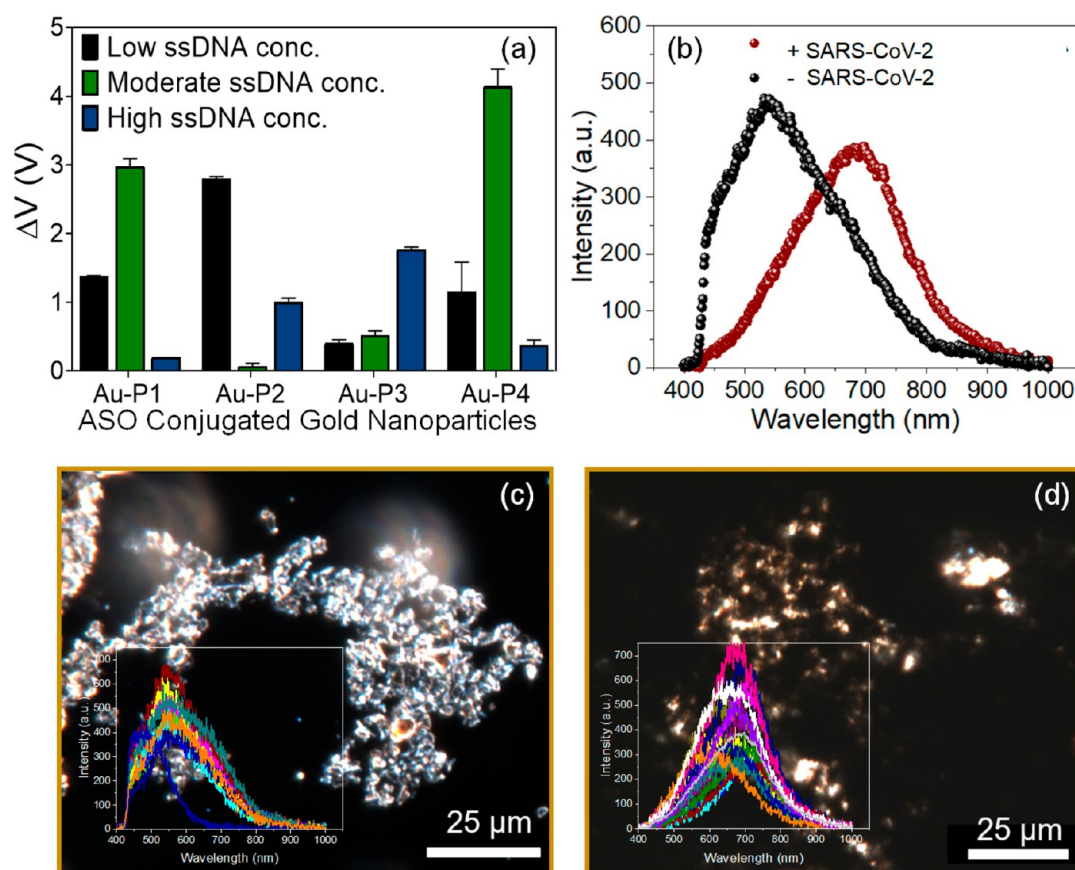


**Figure 4.** (a) Optimization of the antisense ssDNA probes conjugated with AuNPs at different ratios to achieve maximum sensitivity and optimal signal output. (b) Average of the spectra obtained from the hyperspectral imaging from the graphene-Au-P<sub>mix</sub> in the absence and presence of SARS-CoV-2 viral RNA. Enhanced dark-field microscopic-hyperspectral image (EDFM-HSI) of the graphene-Au-P<sub>mix</sub> (c) in the absence of SARS-CoV-2 RNA and (d) in the presence of SARS-CoV-2 RNA with spectra collected from several pixels shown in the inset.

hybridization kinetics of the ssDNA probes with their complementary target can be significantly altered when high densities of ssDNA probes are immobilized. High ssDNA probe density may lead to slower response time or nonlinear sensor response due to the unnecessarily complicated binding behavior, which rises at high probe density.<sup>66</sup> Several experiments have, therefore, been conducted using the electrochemical chip to find the optimum concentration of the ssDNA probe. Three different concentrations of each of the four ssDNA probes (*i.e.*, P1, P2, P3, and P4) were used to cap the AuNPs, and the corresponding electrical performances of the sensors were investigated with a fixed concentration of the viral SARS-CoV-2 RNA load. The three different concentrations were designated as high (H), moderate (M), and low (L) level, which is equivalent to 0.5, 1, and 2  $\mu\text{M}$  of the ssDNA, respectively (see the [Experimental Section](#) for more details).

**Figure 4a** illustrates the electrochemical sensor response for each of the AuNPs functionalized with ssDNA probes toward the viral RNA at three different probes/AuNPs ratio. The moderate ratio of P1 (Au-P1<sub>M</sub>) exhibits the highest change in the signal output, whereas the lowest ratio of P2 (Au-P2<sub>L</sub>) was found to be the optimum concentration for this probe, which shows the highest change in the sensor output compared to other concentrations. On the other hand, the highest ratio of P3 (Au-P3<sub>H</sub>) was found to be the optimum, and finally, the moderate ratio of P4 (Au-P4<sub>M</sub>) provided the best performance. The nanoparticle tracking analysis using ZetaView followed a

similar trend in which the increase in hydrodynamic diameter after the addition of SARS-CoV-2 viral RNA load was found to be the highest for moderate P1 (Au-P1<sub>M</sub>), low P2 (Au-P2<sub>L</sub>), high P3 (Au-P3<sub>H</sub>), and moderate P4 (Au-P4<sub>M</sub>) (**Figure S5**). These constructs, Au-P1<sub>M</sub>, Au-P2<sub>L</sub>, Au-P3<sub>H</sub>, and Au-P4<sub>M</sub>, were then considered to build a sensitive platform for the selective recognition of SARS-CoV-2 viral RNA. The average number of ssDNA probes conjugated to each AuNP has been quantified and found to be 6.05, 5.05, 29.8, and 20.12 for Au-P1<sub>M</sub>, Au-P2<sub>L</sub>, Au-P3<sub>H</sub>, and Au-P4<sub>M</sub>, respectively. Accordingly, all the four probes (*i.e.*, Au-P1<sub>M</sub>, Au-P2<sub>L</sub>, Au-P3<sub>H</sub>, and Au-P4<sub>M</sub>) were mixed (Au-P<sub>mix</sub>) in an equivalent amount with each other to further improve the DNA–RNA hybridization propensity (**Figure S6**) and enhance the analytical sensitivity of the electrochemical sensor toward the selective detection of SARS-CoV-2 viral RNA (**Figure 4a**).

To evaluate the effect of the gold nanoparticles' size on the sensor performance, two additional gold nanoparticles with sizes of  $50 \pm 5$  nm and  $100 \pm 10$  nm have been tested in addition to the original size ( $10 \pm 5$  nm). Each gold nanoparticle has been capped with one of the four ssDNA probes based on the previous optimum value (*i.e.*, Au-P1<sub>M</sub>, Au-P2<sub>L</sub>, Au-P3<sub>H</sub>, and Au-P4<sub>M</sub>). An equal amount of each Au<sub>xnm</sub>-P<sub>x</sub> was mixed to make Au<sub>xnm</sub>-P<sub>mix</sub> and used to make the sensor chip by depositing the mixture on the sensor surface. The response toward  $10^6$  copies/ $\mu\text{L}$  of SARS-CoV-2 viral RNA has been recorded from the sensor chip with Au<sub>10nm</sub>-P<sub>mix</sub>, Au<sub>50nm</sub>-P<sub>mix</sub>, and Au<sub>100nm</sub>-P<sub>mix</sub>. **Figure S7** shows that the 10 nm AuNPs

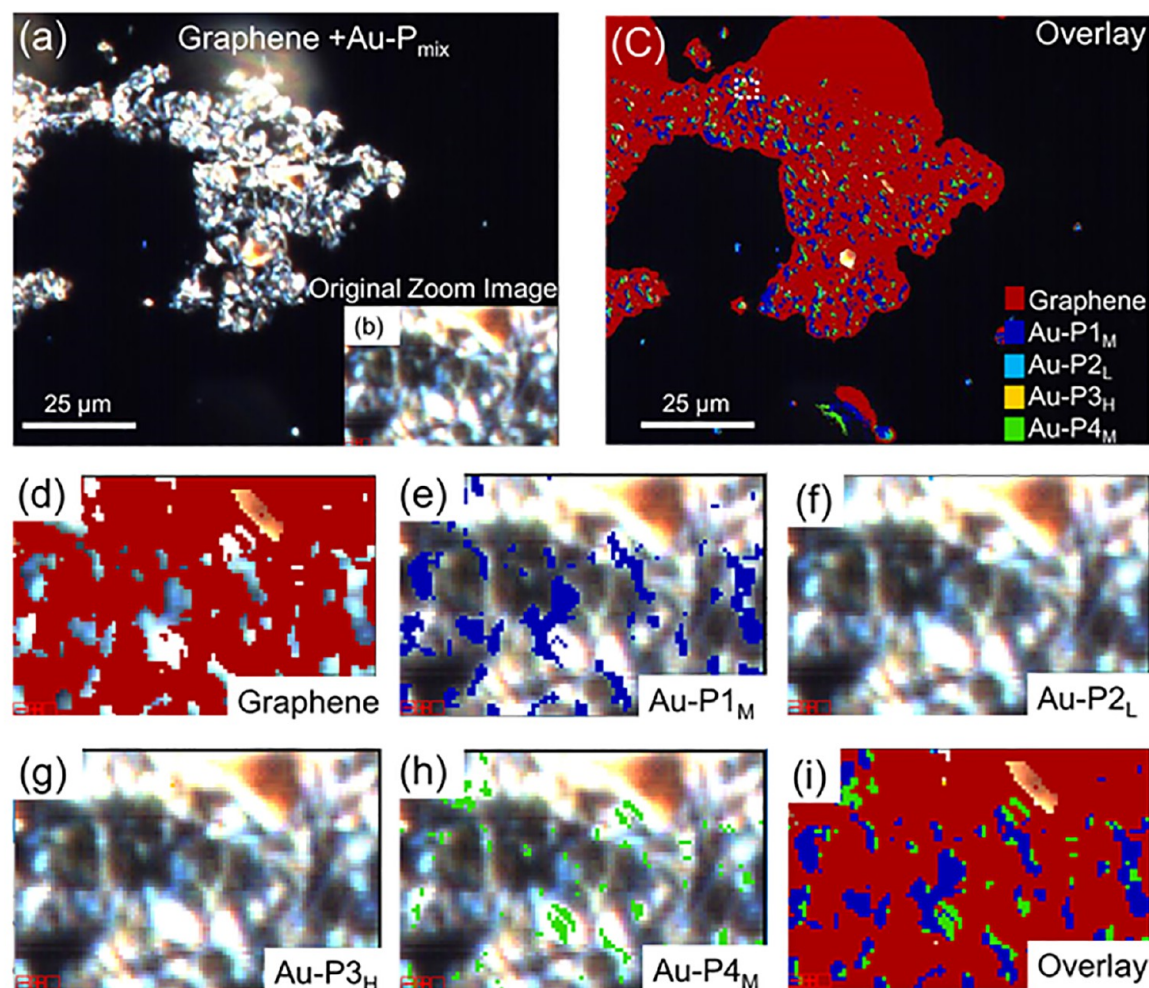


**Figure 5.** (a) Dark-field original image of the graphene-Au-P<sub>mix</sub> sensor chip in the absence of the SARS-CoV-2 RNA. (b) Overlay of the image “map” on the dark-field image in (a). (b, d–i) Zoom-in image in the dotted box of the platform showing the localization of (b) the original dark-field image, (d) graphene nanoplatelet, (e) Au-P<sub>1M</sub>, (f) Au-P<sub>2L</sub>, (g) Au-P<sub>3H</sub>, (h) Au-P<sub>4M</sub>, and (i) overlay of the four Au probes.

exhibit the optimum response compared to the other nanoparticles, 50 and 100 nm in size. It was apparent that larger nanoparticles at sub-nanometer gaps have lower DNA density, in which the DNA density is higher for the small particles and decreases as the nanoparticle size increases.<sup>67</sup> Accordingly, we have received a better response from the smaller sized gold nanoparticles than the larger ones. Further studies are required to fully understand the effect of the size on the sensor response, which is beyond the scope of this first report.

To further confirm the exceptional affinity of the ssDNA probes to the target segment in the viral RNA, an advanced instrumental technique such as hyperspectral spectroscopy was used.<sup>43</sup> Hyperspectral imaging (HSI) is a label-free detection technique that can be used to confine a nanomaterial based on its hyperspectral signature by combining the power of both imaging and spectrophotometry.<sup>68,69</sup> The HSI system is based on the enhanced dark-field microscopic (EDFM) advanced optics combined with a computational algorithm used to capture a spectrum in the range of 400 to 1000 nm at each pixel of the image. Each individual material exhibits a spectrum signature here representing the identity of the material of interest even in a blended sample. Thus, the hyperspectral can be used to create an image “map” to localize the material of

interest in the tested sample. Therefore, EDFM-HSI mapping has widely been confirmed to accurately localize and identify the nanomaterials in samples more efficiently compared to the other conventional approaches.<sup>70,71</sup> To this end, the electrochemical chip—as described before—was prepared on a glass slide and investigated under a hyperspectral imaging microscope to reveal the selectivity and efficient hybridization of the ssDNA probes with the viral RNA at a microscopic level. A red-shift of ~150 nm was observed in the hyperspectral image following the addition of the SARS-CoV-2 RNA to the graphene-Au-P<sub>mix</sub>-based platform (Figure 4b). Figure 4c depicts the dark-field image of the graphene-coated Au-P<sub>mix</sub> platform in the absence of viral RNA, whereas Figure 4d represents the dark-field image of the same platform after the addition of the viral RNA. The shift in the spectral peaks after the addition of the target RNA confirmed the successful hybridization of ssDNA probes with its complementary region in N-gene sequence within the electrochemical sensor chip.

To gain more insight about the localization and distribution of each ssDNA probe-capped gold nanoparticles when bound to the viral RNA, the hyperspectral image mapping has been explored. Figure 5 depicts the localization of Au-P<sub>1M</sub>, Au-P<sub>2L</sub>, Au-P<sub>3H</sub>, and Au-P<sub>4M</sub> within the graphene film before the addition of SARS-CoV-2 viral RNA. In the absence of the



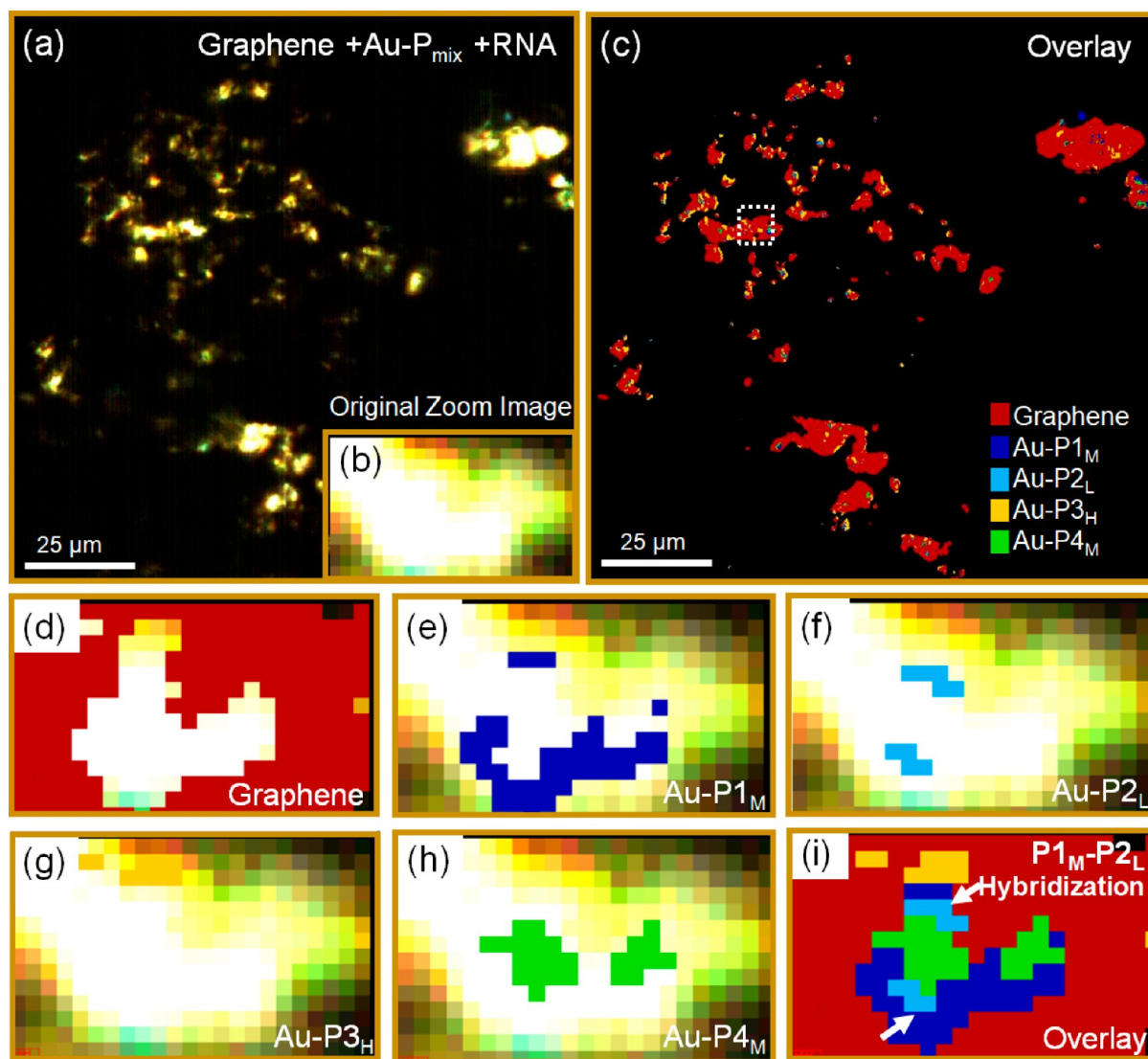


**Figure 6.** (a) Original dark-field image of the graphene-Au-P<sub>mix</sub> in the presence of SARS-CoV-2 viral RNA. (b) Overlaid image “map” on the dark-field image in (a). (b, d–i) Zoomed-in image in the dotted box of the platform showing the localization of (b) the original dark-field image, (d) graphene nanoplatelet, (e) Au-P<sub>1M</sub>, (f) Au-P<sub>2L</sub>, (g) Au-P<sub>3H</sub>, (h) Au-P<sub>4M</sub>, and (i) overlay of the four Au probes.

SARS-CoV-2 RNA, the Au probes are found to be randomly distributed within the graphene film (Figure 5). However, in the presence of the viral RNA, the Au probes are arranged where Au-P1 and Au-P2 were found close to each other, and Au-P3 and Au-P4 were observed to be in proximity (Figure 6), which supports the specific binding of the ssDNA probe to its target. Figure S8 shows a zoomed-in image that illustrates the adjacent Au-P<sub>1M</sub> and Au-P<sub>2L</sub> in the hyperspectral map in the presence of the SARS-CoV-2 RNA, a trend that does not exist in the absence of SARS-CoV-2 RNA. This can be explained based on our design of the ssDNA probes, where P1 and P2 are targeting two consecutive regions in one segment of the SARS-CoV-2 RNA, whereas P3 and P4 are targeting another segment of the N-gene consecutively (Figure 2a). Further, it can be proposed that Au-P1 was found to be the most abundant, followed by Au-P4, Au-P3, and Au-P2 among the ssDNA probe-capped AuNPs while considering the zone where Au probes are accumulated in the presence of SARS-CoV-2 viral RNA (Figure 6). This can be explained from the comparative target RNA sequence binding energies and

binding disruption energies of the four different antisense oligonucleotides (Figure 2d).

Dark-field imaging further confirmed the sensitive and selective binding of SARS-CoV-2 by confirming the formation of a large cluster with Au-P<sub>mix</sub> (Figure S9). However, no obvious aggregate or formation of a large entity has been observed in the presence of MERS-CoV (Figure S10). The UV-vis spectrum also confirmed the sensitivity of the ssDNA-capped AuNPs to the SARS-CoV-2 viral RNA (Figure S11).

Gold nanoparticles have been used extensively as a core element to develop many diagnostic assays.<sup>14,71</sup> Gold nanoparticles can be synthesized with controlled size, high reproducibility, and efficiency, making them an attractive candidate for diagnostic tests. In this work, gold nanoparticles were deposited on the sensor chip surface using the drop-casting method. To evaluate the effect of the gold nanoparticles' distribution on the sensor's analytical performance, we assessed the variation in the sensor response to the same viral load using different sensors; the gold nanoparticles were randomly distributed on each of them. Gold nanoparticles were deposited on the surface of multiple sensor chips from

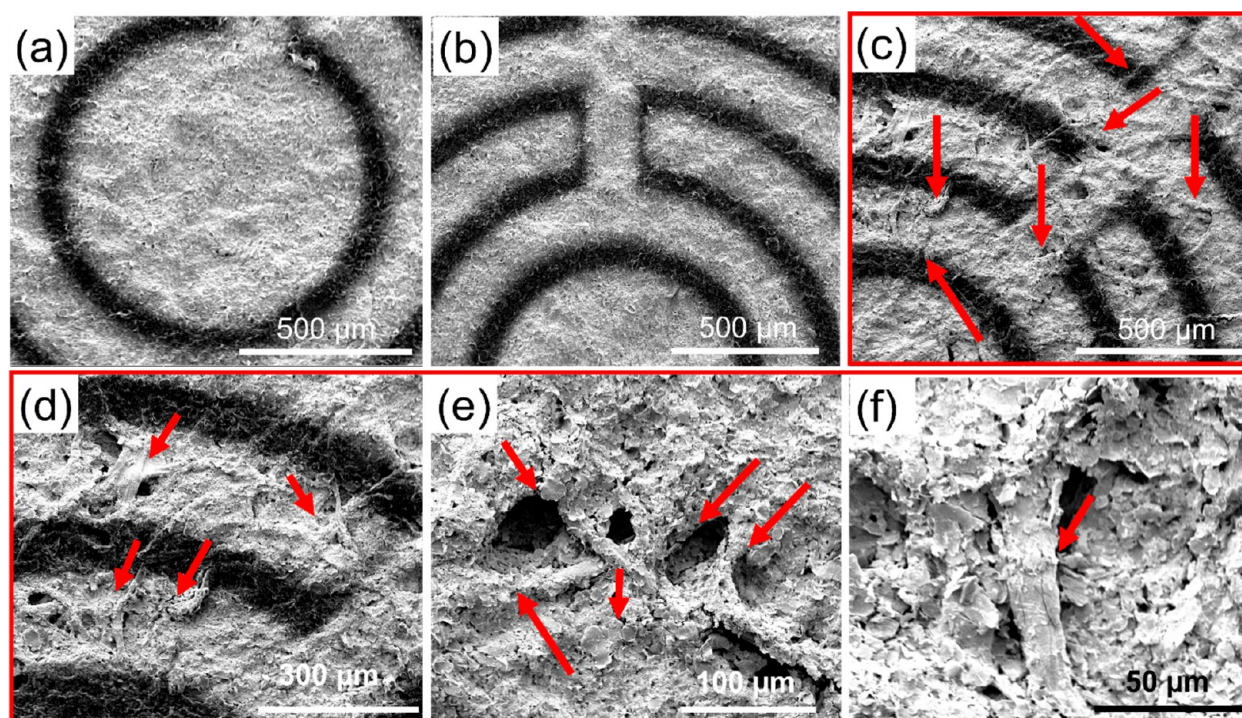


Figure 7. SEM images: (a) sensor without any addition of sample; (b) sample addition with a volume of 10  $\mu\text{L}$ ; and (c) sample addition with a total volume of 12  $\mu\text{L}$ . A zoom-in image of (c) is shown in (d)–(f).

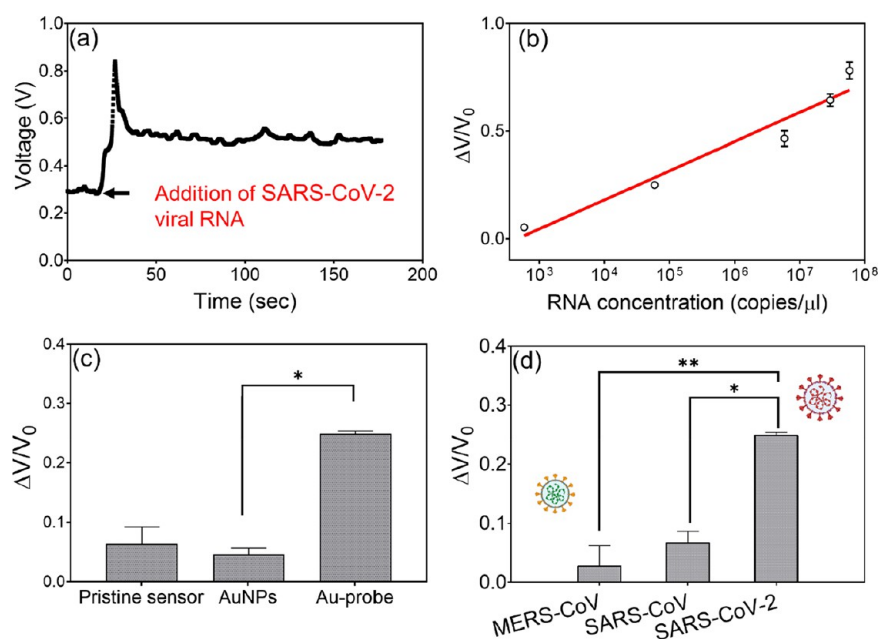


Figure 8. (a) Sensor output signal as a function of time with the addition of SARS-CoV-2 viral RNA load ( $5.85 \times 10^4$  copies/ $\mu\text{L}$ ). (b) The standard curve was obtained from the electrochemical sensor with an increasing concentration of SARS-CoV-2 viral RNA. (c) Comparative electrochemical responses in the presence of SARS-CoV-2 RNA obtained from the pristine sensor, the pristine sensor when deposited with citrate-stabilized gold nanoparticles (AuNPs), and ssDNA-capped AuNPs (Au probe). (d) Relative electrochemical response of the sensor to MERS-CoV and SARS-CoV RNA when compared to SARS-CoV-2 viral RNA.

which the deposition process was independent for each of them. The response of seven sensor chips was recorded against an equal concentration of SARS-CoV-2 RNA ( $\sim 1 \times 10^5$  copies/ $\mu\text{L}$ ). No significant difference was observed between the different sensors. The average response of the seven sensors was found to be 0.23, with a standard deviation of 0.02. These results indicated that the variation in the AuNP

distribution due to the deposition method had no obvious effect on the sensor performance (Figure S12).

**Real-Time Detection of SARS-CoV-2 Viral RNA.** The aim of this work was to develop a POC sensor that is cost-effective and portable and can be integrated with smartphones for easy and rapid diagnosis of SARS-CoV-2. To achieve this, we first eliminated the complex RNA amplification step using



polymerase chain reaction (PCR) or reverse transcription PCR (RT-PCR) and introduced the electrical signal amplification from gold nanoparticles. Further, we eliminated the need for the conventional techniques used for impedance recordings, such as quartz crystal microbalance (QCM), electrochemiluminescence (ECL), cyclic voltammetry (CV), and EIS, and replaced them by a simple signal conditioning circuit, which was integrated with a microcontroller and an algorithm for the computer interface (Figure S13). The real-time recording of electrical signals allowed the sensitive detection of SARS-CoV-2 genetic material in the RNA sample mediated by the optimized RNA–DNA hybridization among the viral RNA and four of the selected Au probes. As illustrated in Figure 1a, the gold nanoparticles capped with ssDNA will be deposited on the surface of the sensor chip by the drop-casting method. To this end, the volume of Au-Px solution deposited on the surface has been optimized to maintain the integrity and avoid the swelling effect of the sensor platform. Figure 7a depicts the SEM image of the sensor chip without the addition of any solution, Figure 7b shows the surface after the addition of 10  $\mu\text{L}$  of the solution, and Figure 7c demonstrates the sensor surface after the addition of 12  $\mu\text{L}$  of solution. The sensor maintains its integrity up to 10  $\mu\text{L}$  of the solution, whereas adding 2  $\mu\text{L}$  of extra solution led to obvious damage to the sensor surface (Figure 7c–f) and swelling in the paper fibers; the paper fibers become visible in the image. Figure S14 depicts the SEM images of fibers in the bare filter paper. In the sensor chip, the paper's fibers are hidden underneath the graphene layer (Figure 7a); the same holds true for the SEM image of the sensor chip after the addition of 10  $\mu\text{L}$  of the solution (Figure 7b) where no obvious swelling signs, such as the appearance of thick fibers or distortion of the graphene configuration, were observed. On the other hand, Figure 7c–f shows a clear sign of paper swelling where the paper fibers become obvious and thicker, causing damage in the sensor chip at the microscopic level. Therefore, 10  $\mu\text{L}$  is the optimum maximum volume that can be added to the sensor chip while maintaining its integrity. An 8  $\mu\text{L}$  amount is found to be sufficient to cover the entire sensor electrode—the circular electrode—and this volume has been adopted for making the sensors throughout this study, with a total number of gold nanoparticles of  $24 \times 10^7$  particles per sensor chip. A clinical sample of 2  $\mu\text{L}$  volume has then been added to ensure the total volume added to the sensor chip did not exceed 10  $\mu\text{L}$ .

It was expected that the ssDNA probes-capped AuNPs selectively bind with its target complementary SARS-CoV-2 RNA sequence and induce aggregation depending on their closely following target sequence positions. In the presence of SARS-CoV-2 RNA, the specific RNA–DNA hybridization led to the change in charge and electron mobility on the graphene surface, which brought the change in sensor output voltage. The change in the sensor electrical signal was observed instantaneously, which reached stability within a short duration of time with an average response time of less than 5 min, as shown in Figure 8a. This illustrates a representative output signal of the sensor chip as a function of time after the addition of SARS-CoV-2 viral RNA. The sensor is composed of a filter paper as a base material that has been coated by graphene nanoplatelets to form a conductive film. The gold electrode has been deposited on the surface of the graphene film as the contact pad for the electrical readout. Finally, gold nanoparticles capped with ssDNA probes specific to the SARS-CoV-2 RNA have been deposited on the sensor surface, which

represents the recognition element of the sensor. In the presence of the SARS-CoV-2 RNA, the ssDNA mounted on the AuNPs' surface hybridized with its complementary target sequence on the surface of the graphene conductive film. The charges at the graphene–solution interface increase due to the hybridization of the viral RNA with the ssDNA sequence, which induces a variation in the graphene potential with a positive drift (eq 1). In order to eliminate the effect of the background noise, the change in the sensor output voltage was normalized to the sensor's initial voltage. The time-series signal was recorded as a response to the addition of the viral RNA sample consisting two main parts, transient and steady-state response. The addition of the RNA sample at a certain time point ( $t$ ) represented a step input. The sensor exhibited a step response, which was represented by a sudden increase of the signal as a sharp peak (transient response). After some time, the sensor reached a steady-state response, which reflected the response to the viral RNA concentrations. This increase in the sensor signal after the addition of the sensor and following partial decrease can be seen in the whole electrochemical platform since it represents both the transient and the steady-state responses of the sensor.<sup>14</sup>

To further investigate the performance of the sensor, the dynamic response of the sensor, when deposited with Au-P<sub>mix</sub>, was evaluated to various concentrations of viral RNA load extracted from Vero cells infected with the SARS-CoV-2 virus. Figure 8b illustrates the linear response (standard curve) of the electrochemical biosensor with increasing concentrations of viral RNA. This fully integrated device successfully exhibited a broad linear detection range from 585.4 copies/ $\mu\text{L}$  to  $5.854 \times 10^7$  copies/ $\mu\text{L}$ , with a sensitivity of  $231 (\text{copies}/\mu\text{L})^{-1}$  for SARS-CoV-2 viral RNA. The sensor sensitivity is referred to as the change in the sensor output per unit change in the sensor input. The sensitivity, by definition, is the ratio of the measured output to the measured analyte or target and can be calculated as the slope of the system transfer function. In our case, the sensitivity is the ratio of the relative change in the sensor voltage ( $\Delta V/V_0$ ) to SARS-CoV-2 RNA concentration (copies/ $\mu\text{L}$ ), which has units of  $(\text{copies}/\mu\text{L})^{-1}$  since  $\Delta V/V_0$  is unitless. One of the important sensor performances is the limit of detection (LOD). The LOD represents the lowest amount of the target substrate that can be distinguished from its absence with a predefined confidence level, usually 99%. The limit of detection is usually calculated based on statistics from the blank measurement points and the slope (analytical sensitivity, as we mentioned earlier) of the sensor standard curve. The limit of detection of the sensor chip has thus been calculated based on  $\text{LOD} = 3.3S_{\text{XY}}/\text{slope}$  and found to be 6.9 copies/ $\mu\text{L}$ . This significantly lower value of the LOD indicated the improved sensitivity and superior analytical performance of the designed device. However, the pristine graphene-based device and the citrate-stabilized AuNPs deposited on the graphene-based device did not show any significant output signal change in the presence of the viral RNA load (Figure 8c). These results supported the importance of ssDNA probes and their sensitivity toward the target SARS-CoV-2 viral N-gene. A control experiment was further conducted to determine the selectivity of the developed COVID-19 biosensor, where the sensor output signal was recorded in the absence of SARS-CoV-2 viral RNA and in the presence of MERS-CoV and SARS-CoV viral RNA load. The sensor, when deposited with Au-P<sub>mix</sub>, showed no significant change in the output signal toward either MERS-CoV or SARS-CoV RNA,



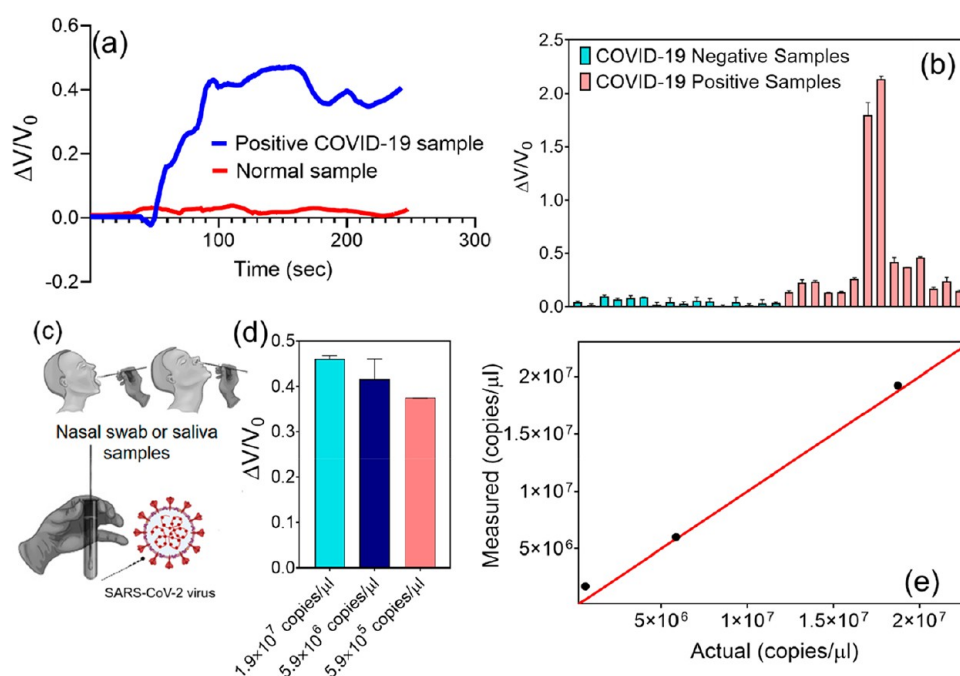


**Figure 9.** (a) Real-time response of the sensor chip toward COVID-19 positive clinical samples and healthy samples. (b) Comparison of the sensor chip response among a representative set of clinical samples from 15 healthy asymptomatic samples and 15 confirmed COVID-19 positive samples. (c) Schematic diagram for the sources of clinical samples that have been collected either from a nasopharyngeal swab or saliva. (d) Analysis and comparison with the actual RNA concentration for three clinical samples. The sensor response toward each clinical sample has been recorded in three repetitive measurements. The average of three measurements has been used to estimate the RNA concentration using (e) the standard curve,  $r^2 = 0.999$ , obtained from standard SARS-CoV-2 genomic RNA samples.

demonstrating the selectivity of the device platform toward SARS-CoV-2 with no obvious cross-reactivity (Figure 8d).

**Selective Detection of SARS-CoV-2 in Clinical Samples.** Finally, we evaluated the performance of the developed sensor chip in detecting the presence of SARS-CoV-2 RNA in clinical samples (Figure 9). Nasopharyngeal swab specimens have been collected from COVID-19 patients and healthy asymptomatic subjects and stored in viral transfer medium (VTM) for future use (Figure 9c). The results were benchmarked with a gold standard SARS-CoV-2 diagnostic kit known as LabGun COVID-19 RT-PCR kit (FDA approved).<sup>72</sup> Prior to testing of patient samples, we investigated the sensor response toward samples that were collected from healthy asymptomatic subjects, confirmed using RT-PCR. Figure 9a clearly shows that the sensor responds to the positive COVID-19 confirmed samples selectively and demonstrated a significant increase in sensor voltage compared to the negative samples. Thus, the sensor chip clearly discriminated between COVID-19 positive samples and healthy negative samples in a rapid manner.

The sensor showed a negligible response toward the samples collected from a healthy individual, while a high relative change in the sensor chip voltage was observed for the positive COVID-19 confirmed clinical samples (Figure 9b). Moreover, the sensor chip responded to COVID-19 positive samples with different viral RNA loads of  $1.9 \times 10^7$ ,  $5.9 \times 10^6$ , and  $5.9 \times 10^5$  (Figure 9d). Quantitative detection of the viral RNA load using a simple sensor chip is also important in monitoring the progression of SARS-CoV-2 infection after confirming the disease after the onset of symptoms.<sup>73</sup> To this end, we evaluated the ability of the developed sensor chip to quantify the viral RNA load. The RNA concentration of the tested COVID-19 positive clinical samples (*i.e.*, viral RNA load of  $1.9$

$\times 10^7$ ,  $5.9 \times 10^6$ , and  $5.9 \times 10^5$ ) was estimated with high accuracy (Figure 9e), where the RNA concentration of the clinical samples that were back-calculated from the standard curve was found to be highly correlated with the actual RNA concentration with Pearson's correlation of  $r = 0.999$ .

Finally, the sensor response toward the collected clinical samples has been used to distinguish the positive COVID-19 samples from the negative ones—YES/NO answer—using the thresholding process. The sensor response—relative change in the sensor voltage ( $\Delta V/V_0$ )—has been classified by applying a threshold value of 0.13, in which the samples giving a response higher than the threshold are considered as positive, whereas the samples with a response lower than 0.13 are assigned as negative. Figure 10a illustrates the sensor chip response toward the 48 clinical samples; the samples that belong to the negative group all showed a response ( $\Delta V/V_0$ ) less than 0.13. On the other hand, the samples that showed a response higher than 0.13 belong to the COVID-19 positive group. Table S2 summarizes the amount of SARS-CoV-2 RNA in each clinical sample in copies/ $\mu$ L. Figure 10b shows the confusion matrix, which summarized the performance of the sensor chip in identifying the COVID-19 positive and negative samples, by benchmarking the results to a gold-standard technique for SARS-CoV-2 diagnosis known as the LabGun COVID-19 RT-PCR diagnosis kit (FDA EUA approved).<sup>72</sup> The sensor was thus able to correctly assign the positive and negative samples to their respective groups with almost 100% accuracy, specificity, and sensitivity (Figure 10b). It is worth mentioning that this threshold value is not universal and may be subject to change with an increasing number of tested clinical samples.

On the basis of the results obtained from the current study, we may conclude that ssDNA-capped AuNPs as a sensing element amplified the electrical signal, while the use of ssDNA

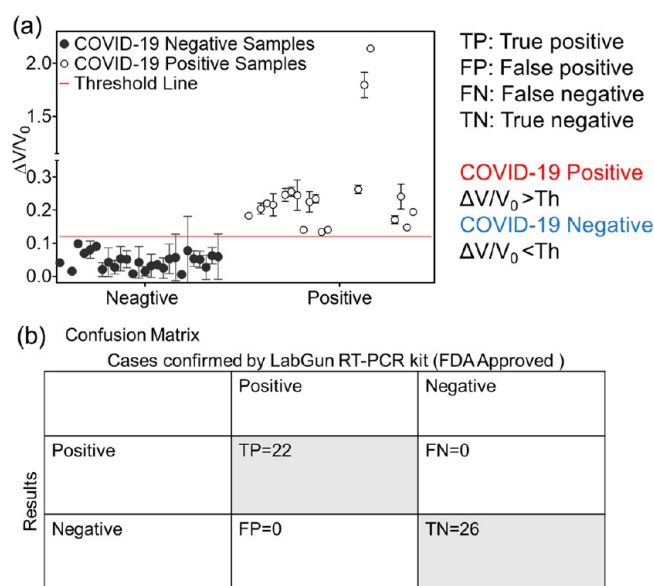


**Figure 10.** (a) Summary of the results of classifying 48 clinical samples into COVID-19 positive or negative cases using the developed sensor chip, which was benchmarked to the standard SARS-CoV-2 diagnostic kit (LabGun COVID-19 RT-PCR kit). (b) Confusion matrix of the classification results obtained by applying thresholding (threshold = 0.13) on the sensor chip response against the 48 clinical samples.

probes provided an enhanced selective output response only in the presence of SARS-CoV-2 viral RNA. To design the electrochemical biosensor, ssDNA-capped AuNPs (Au probe) were drop-cast on a finely suspended graphene-coated filter paper. The electron transfer process was enhanced by utilizing gold nanoparticles, which provided a large surface area to conjugate ssDNA probes and thus improved the electrochemical response of the device enormously for the target SARS-CoV-2, with no significant response to the lack of target. To enhance the sensor sensitivity, the concentrations of the four carefully designed ssDNA probes were optimized to achieve an improved electrical response. Under this optimal condition, the developed sensor chip demonstrated the ability to detect viral COVID-19 RNA in a wide linear range from 585.4 copies/ $\mu\text{L}$  to  $5.854 \times 10^7$  copies/ $\mu\text{L}$ , with a significantly lower detection limit of 6.9 copies/ $\mu\text{L}$ . The ssDNA-capped AuNPs provided an enhanced signal in response to its target, presumably due to the selective hybridization of the ssDNA probes with their complementary sequences in four different segments of the same N-gene. Compared to the ssDNA-conjugated sensor chip or pristine graphene chip, the ssDNA-capped AuNPs-graphene-based sensor chip showed an enhanced electrical response to the target with no obvious electric response toward the scrambled RNA. This enhanced sensitivity of the present sensor configuration can thus be explained by three possible reasons: suitably designed ssDNA probes, the signal amplifying gold nanoparticles, and the conductive graphene nanoplatelet film. The high carrier mobility ( $>2000 \text{ cm}^2 \text{ V}^{-1} \text{ s}^{-1}$ ) of graphene provided enough sensitivity and adsorption capability of the charged analytes at its surface.<sup>74</sup> Thus, the combination of graphene-ssDNA-AuNPs constructs made the electrochemical biosensor platform an ideal candidate for rapid and accurate diagnosis of positive COVID-19 cases. Further, the design of the antisense probes to simultaneously target two regions of the SARS-CoV-

2 N-gene ensured the reliability and feasibility of the sensor even if one region of the viral gene undergoes mutation during its current cross-transmission. The applicability of the proposed sensor chip was also evaluated successfully using SARS-CoV-2 viral RNA samples based on signal amplification methodology mediated by the change in resistance. Linearity was achieved in a broad range of RNA concentrations from 585.4 copies/ $\mu\text{L}$  to  $5.854 \times 10^7$  copies/ $\mu\text{L}$ . It was understood that viral RNA detection is more reliable than antibody detection due to the improved accuracy, specificity, and ability of the current sensor to reduce false positive or negative responses, as well as the fast diagnostic time frame after infection. The performance of the sensor chip has been evaluated using clinical samples from positive COVID-19 confirmed cases and healthy asymptomatic cases. Given that the tested clinical samples include RNA from various sources, including SARS-CoV-2, which are responsible for generating noise signals, the sensor limit of detection, which is 6.9 copies/ $\mu\text{L}$ , is low enough to use in clinical practice. Table S3 summarizes most of the peer-reviewed SARS-CoV-2 virus detection technologies. In comparison, our technology is devoid of any requirements for advanced instrumental facilities. Moreover, the detection time taken by the existing state-of-the-art approaches is either days or multiple hours. Our technology is on par with the existing technologies with a test result time of  $\sim 5$  min. Additionally, the major limitation of the antibody-based approach (lateral flow assays) is also addressed as the extent of infection is determined by detecting the presence of a virus and not just evidence of the virus being in the body. In short, the technology reported here addresses the shortcomings of the existing COVID-19 sensors in a POC setting with a quicker sensing period without the need for any advanced instrumental techniques, modern laboratory infrastructural facilities, and the involvement of experienced researchers without compromising the specificity and sensitivity.

The applications of electrochemical-based genosensors are far-reaching. The sensor, when integrated with a benchtop device, could potentially be used as a POC test in low-resource settings. The ability of the developed graphene-based electrochemical sensor to detect the presence of viral RNA in a cost-effective and reusable method could be applied at home as well as in the doctor's office. The base unit will comprise the electrical components (microcontrollers, LED screen, Bluetooth, and Wi-Fi modules) as well as algorithms necessary to perform a POC test using the interfaced sensor. Furthermore, the base device can be supported by future software updates for the algorithms to perform multiplexed sensing to differentiate between different viral strains (e.g., influenza from SARS-CoV-2) to provide an effective diagnosis. The sensor could be priced at  $\sim \$10$  per sensor.

Currently, the gold standard test for diagnosing COVID-19 is a PCR test where a healthcare worker collects samples and ships them to a lab for a confirmatory test. A healthcare worker equipped with a sensor with preaffixed probes associated with SARS-CoV-2 viral RNA could eliminate the need for a preliminary, and the sensor could be regarded as an accurate confirmatory test, reducing backlogs in the laboratories. Another aspect of the developed sensor could be where a person at home would purchase a kit that has the probes associated with SARS-CoV-2 viral RNA and deposit a sample of treated saliva onto the sensor. If the sensor detects an elevated presence of a known viral RNA that is associated with

COVID-19, then that person would be able to go to the doctor and seek further screening tests and therapeutic interventions. The sensor would be an effective tool in screening symptomatic as well as asymptomatic COVID cases. Furthermore, the same approach could be used at the doctor's office as a confirmatory test for the presence of other pathogenic bacterial and viral DNA/RNA. This would help the medical community to more effectively diagnose and fight off the spread of current as well as future viral infections.

**Conclusion.** Briefly, we developed herein an electrochemical platform made up of graphene and gold nanoparticles conjugated with suitably designed antisense oligonucleotides for the rapid, accurate, selective, and ultrasensitive detection of SARS-CoV-2 viral RNA within a time period of less than 5 min. Four of the antisense ssDNA probes were used to cap AuNPs at an optimized concentration to target the viral N-gene (nucleocapsid phosphoprotein) selectively. Hyperspectral microscopic results evidenced the sensitivity and the selectivity of the designed ssDNA probes toward the target SARS-CoV-2 viral RNA. The sensitivity and analytical performance of the device were evaluated both in the absence and in the presence of gold nanoparticles when conjugated with either citrate or antisense oligonucleotides. The results showed the improved electrochemistry of the device only when deposited with the ssDNA-capped AuNPs. Further, the selectivity of the device was demonstrated with SARS-CoV and MERS-CoV viral RNA. This fully integrated device successfully exhibited a broad linear detection range from 585.4 copies/ $\mu\text{L}$  to  $5.854 \times 10^7$  copies/ $\mu\text{L}$ , with a sensitivity of 231 (copies  $\mu\text{L}^{-1}$ ) $^{-1}$ . The sensor exhibits a limit of detection of 6.9 copies/ $\mu\text{L}$  without nucleic acid amplification, where the value achieved for the LOD is quite comparable with the current clinical approaches. The advantages of the developed biosensor over previously reported tests therefore include an improved limit of detection, no need for additional redox medium for electron exchange, faster response to achieve stable data, excellent shelf life, and its plausible economic production. The design of the ssDNA probes to simultaneously target two regions of SARS-CoV-2 N-gene ensures the feasibility and reliability of the sensor even if one region of the viral gene undergoes mutation during its current spread. In addition to this, the current methodology overcomes the limitations of widely used antibody-based serological tests, as the developed test can detect the early stage of infection. Moreover, the developed platform can also be adapted to detect other viruses, which makes it a universal platform. Finally, clinical samples collected from both COVID-19 positive patients and healthy asymptomatic subjects have been used to evaluate the sensor performance. The sensor chip shows a significant change as a response to COVID-19 positive samples, whereas an insignificant change has been observed as a response to the healthy subjects' samples, with a classification accuracy of nearly 100%. Thus, the present device does not require the ongoing traditional approach of amplifying cDNA from the extracted RNA from the patients' bodily fluids and utilization of the cDNA for the detection of COVID-19. In contrast, the current approach addresses the issue based on signal amplification methodology mediated by the change in output voltage. Currently, we are integrating the device with a portable mobile platform, which can be easily translated for the rapid diagnosis of positive COVID-19 cases.

## MATERIALS AND METHODS

**Reagents.** All the materials were procured from widely known commercial distributors. The custom-designed thiol-conjugated ssDNA was purchased from GenScript and stored at  $-20\text{ }^{\circ}\text{C}$  for future use. All the experiments were carried out at a constant room temperature of  $25\text{ }^{\circ}\text{C}$  unless otherwise specified. Vero cells were purchased from ATCC (Vero E6; ATCC CRL-1586). The gamma-irradiated cell lysate and supernatant from Vero E6 cells infected with either SARS-CoV-2, isolate USA-WA1/2020, or the Middle East respiratory syndrome coronavirus (MERS-CoV), EMC/2012, were obtained from BEI Resources, NIAID, NIH.

**Prediction of ssDNA Probes.** The design of the ssDNA has been carried out based on a previous report from our research group.<sup>43</sup> Briefly, the software Soligo<sup>75</sup> was used to predict the antisense oligonucleotide probes specific for the N-gene sequence of SARS-CoV-2. The prediction run was continued at a folding temperature of  $37\text{ }^{\circ}\text{C}$  and ionic conditions of 1 M sodium chloride. The probes are predicted for a preferred length of 20 nucleotide bases. The target binding energies of the antisense probes were then compared among the predicted ones with a binding energy cutoff of  $\leq -8$  kcal/mol.

**Synthesis of Citrate-Capped Gold Nanoparticles.** A solution of sodium citrate (2.2 mM) was taken in ultrapure water (150 mL) and boiled to reflux for 15 min with continuous stirring. A solution of chloroauric acid (1 mL, 25 mM) was then added to the refluxing solution. The solution was stirred for a duration of 20 min. The resulting citrate-stabilized gold nanoparticles were well suspended in water.<sup>52</sup>

**Formation of ssDNA-Capped AuNPs.** The citrate-stabilized AuNPs with a concentration of  $\sim 3 \times 10^{10}$  particle/mL, as measured by ZetaView, were treated with four of the antisense probes separately at three different concentrations of 0.5, 1, and 2  $\mu\text{M}$ , respectively. The mixture was then kept at room temperature for 30 min with constant stirring. The exchange between thiol and citrate groups is expected to take place in this duration. The uncapped ssDNA probe was then removed from the solution by centrifugation at 20 000 rcf for 15 min. The residue was finally resuspended in an equivalent volume of water. Thus, 12 separate samples were prepared for the four ssDNA probes at three different concentrations. These particles are named Au-P<sub>xL</sub>, Au-P<sub>xM</sub>, and Au-P<sub>xH</sub> where  $x$  defines the number of probes and L, M, and H are representative of low (0.5  $\mu\text{M}$ ), medium (1  $\mu\text{M}$ ), and high (2  $\mu\text{M}$ ) concentrations of probes, respectively. The as-synthesized nanoparticles were kept at  $4\text{ }^{\circ}\text{C}$  for future use. The gel electrophoresis experiment was conducted to confirm the capping of thiolated ssDNA probes onto the AuNPs. A 10% glycerol solution was used with the suspension of citrate-stabilized AuNPs and ssDNA-capped Au-P1, Au-P2, Au-P3, and Au-P4. These materials were loaded on 0.5% agarose gel in 0.5 $\times$  Tris-borate-ethylenediaminetetraacetic acid buffer (TBE buffer). The gel was run in a Wide Mini-Sub Cell GT horizontal electrophoresis system (Biorad) at 100 V for 60 min. The number of ssDNA conjugated to each gold nanoparticle was also quantified using a QuantiFluor ssDNA system (Promega Corporation) based on the manufacturer's protocol. The dye selectively binds to the ssDNA strand. Accordingly, fluorescence was recorded from both the treated concentration of ssDNA and the residual concentration of ssDNA in the supernatant after their binding with AuNPs. The fluorescence was monitored through a Biotek Neo fluorimeter using an excitation wavelength of 492 nm and emission at 528 nm.

**Cell Culture.** *Cercopithecus aethiops* kidney epithelial cells (Vero E6) were cultured in Eagle's minimum essential medium at standard conditions with the supplementation of 10% fetal bovine serum at  $37\text{ }^{\circ}\text{C}$ . The culture was maintained by trypsinization of the cells with 0.25% (w/v) trypsin–0.53 mM EDTA solution.

**Isolation of RNA.** Severe acute respiratory syndrome-related coronavirus (SARS-CoV-2), isolate USA-WA1/2020, NR-52287, was obtained from BEI Resources, NIAID, NIH. The sample consists of a crude preparation of gamma-irradiated cell lysate and supernatant from Vero cells infected with SARS-CoV-2 isolate. Separately, NR-50549 consisting of a gamma-irradiated cell lysate and supernatant



from Vero cells infected with MERS-CoV, EMC/2012, was obtained from BEI Resources, NIAID, NIH.

The Vero cells before and after the viral infection were lysed by the addition of TRIzol reagent (1 mL) and aspirated. The total RNA was then extracted and purified from the cell lysate, and the RNA concentration was measured by a Nanodrop. The purified SARS-CoV-2 and MERS-CoV viral RNA concentrations were found to be 35.9 and 4 ng/ $\mu$ L, respectively, with the RNA concentration of noninfected Vero cells being 92.6 ng/ $\mu$ L.

**Fabrication of the Electrochemical Biosensor.** Graphene nanoplatelets (GNPs) and molecular biology grade water were purchased from STREM Chemicals, USA, and Sigma-Aldrich, respectively. Briefly, GNPs with a width of  $\sim$ 6–8 nm and length of about 25  $\mu$ m (100 mg) were added to 10 mL of molecular biology grade water to prepare a suspension. The resulting suspension was probe sonicated at 37 °C at an amplitude of 4, with a pulse rate of 5 s on and 1 s off for 8 cycles ( $\sim$ 4 h) with intermittent cycles of 30 min. To increase the uniformity of resulting mixture over filter paper (Whatman filter paper  $\sim$ 90 mm) with minimum surface defects, a spin-coating technique (Laurell Technologies, North Wales, PA, USA) was utilized at 150 rpm for 45 s, 300 rpm for 600 s, and 600 rpm for 120 s. The spin-coated filter papers were then dried for 10 min under continuous nitrogen flow and dried overnight under a vacuum desiccator at room temperature. Finally, an electron beam evaporator (Temescal Systems FC-2000, Livermore, CA, USA) was used to deposit the micro-Au electrodes with a thickness of 50 nm using a shadow mask with a predefined pattern. The shadow mask design was initially created in AutoCAD 2014 and printed at the facility of Photo-Sciences Inc., Torrance, CA, with a thickness of 0.025 mm on a nickel-brass.

**Protocol for Sample Standardization.** The as-synthesized antisense probe stabilized AuNPs were first sonicated in a bath sonicator for 5 min at room temperature before each use. The solutions are then vortexed for 2 min, and the individual antisense probe-capped AuNPs, 8  $\mu$ L from each solution, were added on top of the gold electrode. The sensor chip was left at room temperature for 30 min with no sign of moisture. On the other hand, for the preparation of  $P_{\text{mix}}$ , equivalent portions from each of the probes ( $P_{1M}$ ,  $P_{2L}$ ,  $P_{3H}$ , and  $P_{4M}$ ) were taken, mixed, and vortexed properly; that is, for a solution of 8  $\mu$ L of  $P_{\text{mix}}$ , 2  $\mu$ L from each of the selected probe formulations was taken. The RNA samples (2  $\mu$ L) with different concentrations were then added on top of the electrodes.

**Electrochemical Data.** The current–voltage electrochemical data were collected using a homemade circuit consisting of a signal conditioner circuit and microcontroller. Each of the individual experiments was repeated at least six times, and an average value of the same has been reported. The obtained signals have been used to evaluate sensor performance. The limit of detection has been calculated based on the following equation:  $\text{LOD} = 3.3S_{\text{xy}}/\text{slope}$ .

**Absorbance Spectra.** The absorbance spectra were recorded with a VWR UV–vis spectrophotometer.

**Measurement of Hydrodynamic Diameter.** The hydrodynamic diameters of the particles were monitored on a particle tracking analyzer (ZetaView Particle Metrix). The hydrodynamic diameters of ODN-capped AuNPs before and after the addition of RNA  $5.854 \times 10^4$  were measured in triplicate.

**Raman Spectroscopy.** The paper-based electrochemical sensor was placed on a microscope glass slide and imaged using a fiber-optic probe with an integrated 532 nm Raman filter set; the probe was connected to a portable Raman spectrometer (Yvon Jobin LabRam ARAMIS).

**Hyperspectral Microscopy.** A film of graphene—as previously described in the sensor chip synthesis protocol—was deposited on a glass slide. Next, a mixture of the gold nanoparticles capped with the four ssDNA probes ( $P_{\text{mix}}$ ) was deposited on the graphene film to mimic the sensor chip. The dark-field imaging and hyperspectral data were recorded with dark-field optical microscope (CytoViva) system of the graphene film alone, with the ssDNA-capped gold nanoparticles in the absence of the COVID-19 viral RNA and after the addition of 1 ng/mL of SARS-CoV-2 RNA.

**Cross-Reactivity Experiment.** We have obtained formaldehyde- and UV-inactivated, purified, SARS coronavirus (NR-3883) from BEI Resources and isolated the viral RNA using the manufacturer's protocol as detailed in the Zymo Research Quick-RNA viral kit (R1035). The extracted RNA was tested using the developed sensor chip.

**Experimental Setup and Real-Time Monitoring.** The fabricated sensors were interfaced with an in-house-built benchtop electrical circuit. The electrical circuit is composed of an Arduino UNO. The microcontroller (ATmega328P) was reconfigured to control the input voltage of 5 V, and a laptop was used to record the data in real time (Figure S15).

**Preparation of Clinical Samples.** The clinical samples tested in this work were collected as part of the registered protocols approved by the Institutional Review Board (IRB) of the University of Maryland, Baltimore. Samples of nasopharyngeal swabs were stored in viral transfer media. The clinical samples were heat-inactivated by heating the samples at 65 °C for 30 min, and then the samples were stored at  $-80$  °C for future use.

**Procedure for the LabGun RT-PCR Assay.** The LabGun COVID-19 RT-PCR kit is optimized to detect RNA from SARS-CoV-2 in nasopharyngeal swabs collected from patients with signs and symptoms of COVID-19. Briefly, nucleic acids were first isolated and purified by the QIAamp viral RNA mini extraction kit. The purified genetic material was then amplified using the LabGun COVID-19 RT-PCR kit. During the PCR extension phase, the probe was degraded by the 5' nuclease activity of Taq polymerase, resulting in the reporter dye being differentiated from the quencher dye. This induces an increase in fluorescence emission. At each cycle, more reporter dye molecules are cleaved from their probes and increase fluorescence. The increase in fluorescence intensity is generally monitored at each PCR cycle by the RT-PCR instrument. It is expected that the samples without the presence of SARS-CoV-2 would not provide any significant increase in emission, while only the COVID-19 positive samples reflect an increment in fluorescence intensity.

## ASSOCIATED CONTENT

### Supporting Information

The Supporting Information is available free of charge at <https://pubs.acs.org/doi/10.1021/acsnano.0c06392>.

Figures S1–S14, Table S1–S3, and associated references (PDF)

## AUTHOR INFORMATION

### Corresponding Author

Dipanjana Pan — Bioengineering Department, University of Illinois at Urbana–Champaign, Urbana, Illinois 61801, United States; Departments of Diagnostic Radiology and Nuclear Medicine and Pediatrics, Center for Blood Oxygen Transport and Hemostasis, University of Maryland Baltimore School of Medicine, Baltimore, Maryland 21201, United States; Department of Chemical, Biochemical and Environmental Engineering, University of Maryland Baltimore County, Baltimore, Maryland 21250, United States; [orcid.org/0000-0003-0175-4704](https://orcid.org/0000-0003-0175-4704); Email: [dipanjana@som.umaryland.edu](mailto:dipanjana@som.umaryland.edu)

### Authors

Maha Alafeef — Bioengineering Department, University of Illinois at Urbana–Champaign, Urbana, Illinois 61801, United States; Departments of Diagnostic Radiology and Nuclear Medicine and Pediatrics, Center for Blood Oxygen Transport and Hemostasis, University of Maryland Baltimore School of Medicine, Baltimore, Maryland 21201, United States; Biomedical Engineering Department, Jordan University of Science and Technology, Irbid 22110, Jordan

**Ketan Dighe** — Bioengineering Department, University of Illinois at Urbana—Champaign, Urbana, Illinois 61801, United States; Department of Chemical, Biochemical and Environmental Engineering, University of Maryland Baltimore County, Baltimore, Maryland 21250, United States

**Parikshit Moitra** — Departments of Diagnostic Radiology and Nuclear Medicine and Pediatrics, Center for Blood Oxygen Transport and Hemostasis, University of Maryland Baltimore School of Medicine, Baltimore, Maryland 21201, United States; [orcid.org/0000-0002-7679-7859](https://orcid.org/0000-0002-7679-7859)

Complete contact information is available at:  
<https://pubs.acs.org/10.1021/acsnano.0c06392>

## Author Contributions

\*M. Alafeef, K. Dighe, and P. Moitra contributed equally to this work.

## Notes

The authors declare the following competing financial interest(s): Prof Pan is the founder or co-founder for three university based start-ups. None of these entities, however, supported this work.

## ACKNOWLEDGMENTS

The authors gratefully acknowledge the receipt of funding from the National Institute of Biomedical Imaging and Bioengineering (NIBIB) R03EB028026, R03 EB028026-02S2, and R03 EB028026-02S1, the University of Maryland, Baltimore (UMB), and University of Maryland, Baltimore County (UMBC). Fabrication of Au electrodes and spin coating of the graphene nanoplatelet suspension were performed at the Frederick Seitz Materials Research Laboratory (MRL), the University of Illinois at Urbana—Champaign (UIUC). Raman spectroscopy experiments have been conducted at the Surface Analysis Center at the University of Maryland, College Park (UMD). The authors would like to thank Prof. Zubair Ahmed's Lab from the Department of Otorhinolaryngology-Head and Neck Surgery, UMB, for providing access to the PCR machine. The following reagents were deposited by the Centers for Disease Control and Prevention and obtained through BEI Resources, NIAID, NIH: (i) SARS-related coronavirus 2, isolate USA-WA1/2020, gamma-irradiated, NR-52287, and (ii) the Middle East respiratory syndrome coronavirus (MERS CoV), EMC/2012, irradiated infected cell lysate, NR-50549.

## REFERENCES

- (1) Chan, K. R.; Wang, X.; Saron, W. A. A.; Gan, E. S.; Tan, H. C.; Mok, D. Z. L.; Zhang, S. L.-X.; Lee, Y. H.; Liang, C.; Wijaya, L.; Ghosh, S.; Cheung, Y. B.; Tannenbaum, S. R.; Abraham, S. N.; St John, A. L.; Low, J. G. H.; Ooi, E. E. Cross-Reactive Antibodies Enhance Live Attenuated Virus Infection for Increased Immunogenicity. *Nat. Microbiol.* **2016**, *1*, 16164.
- (2) Sun, F.; Ganguli, A.; Nguyen, J.; Brisbin, R.; Shanmugam, K.; Hirschberg, D. L.; Wheeler, M. B.; Bashir, R.; Nash, D. M.; Cunningham, B. T. Smartphone-Based Multiplex 30-minute Nucleic Acid Test of Live Virus from Nasal Swab Extract. *Lab Chip* **2020**, *20*, 1621–1627.
- (3) Broughton, J. P.; Deng, X.; Yu, G.; Fasching, C. L.; Servellita, V.; Singh, J.; Miao, X.; Streithorst, J. A.; Granados, A.; Sotomayor-Gonzalez, A.; Zorn, K.; Gopez, A.; Hsu, E.; Gu, W.; Miller, S.; Pan, C.-Y.; Guevara, H.; Wadford, D. A.; Chen, J. S.; Chiu, C. Y. CRISPR–Cas12-Based Detection of SARS-CoV-2. *Nat. Biotechnol.* **2020**, *38*, 870–874.

- (4) Morales-Narváez, E.; Dincer, C. The Impact of Biosensing in a Pandemic Outbreak: COVID-19. *Biosens. Bioelectron.* **2020**, *163*, 112274.
- (5) Fauci, A. S.; Lane, H. C.; Redfield, R. R. COVID-19 — Navigating the Uncharted. *N. Engl. J. Med.* **2020**, *382*, 1268–1269.
- (6) Velavan, T. P.; Meyer, C. G. The COVID-19 Epidemic. *Trop. Med. Int. Health* **2020**, *25*, 278–280.
- (7) Phan, T. Genetic Diversity and Evolution of SARS-CoV-2. *Infect., Genet. Evol.* **2020**, *81*, 104260.
- (8) Huang, C.; Wang, Y.; Li, X.; Ren, L.; Zhao, J.; Hu, Y.; Zhang, L.; Fan, G.; Xu, J.; Gu, X.; Cheng, Z.; Yu, T.; Xia, J.; Wei, Y.; Wu, W.; Xie, X.; Yin, W.; Li, H.; Liu, M.; et al. Clinical Features of Patients Infected with 2019 Novel Coronavirus in Wuhan, China. *Lancet* **2020**, *395*, 497–506.
- (9) Wang, C.; Yu, H.; Horby, P. W.; Cao, B.; Wu, P.; Yang, S.; Gao, H.; Li, H.; Tsang, T. K.; Liao, Q.; Gao, Z.; Ip, D. K. M.; Jia, H.; Jiang, H.; Liu, B.; Ni, M. Y.; Dai, X.; Liu, F.; Van Kinh, N.; Liem, N. T.; et al. Comparison of Patients Hospitalized with Influenza A Subtypes H7N9, H5N1, and 2009 Pandemic H1N1. *Clin. Infect. Dis.* **2014**, *58*, 1095–1103.
- (10) Gandhi, M.; Yokoe, D. S.; Havlir, D. V. Asymptomatic Transmission, the Achilles' Heel of Current Strategies to Control COVID-19. *N. Engl. J. Med.* **2020**, *382*, 2158–2160.
- (11) Kissler, S. M.; Tedijanto, C.; Goldstein, E.; Grad, Y. H.; Lipsitch, M. Projecting the Transmission Dynamics of SARS-CoV-2 Through the Postpandemic Period. *Science* **2020**, *368*, 860–868.
- (12) Udugama, B.; Kadhiresan, P.; Kozłowski, H. N.; Malekjahani, A.; Osborne, M.; Li, V. Y. C.; Chen, H.; Mubareka, S.; Gubbay, J. B.; Chan, W. C. W. Diagnosing COVID-19: The Disease and Tools for Detection. *ACS Nano* **2020**, *14*, 3822–3835.
- (13) Carter, L. J.; Garner, L. V.; Smoot, J. W.; Li, Y.; Zhou, Q.; Saveson, C. J.; Sasso, J. M.; Gregg, A. C.; Soares, D. J.; Beskid, T. R.; Jervey, S. R.; Liu, C. Assay Techniques and Test Development for COVID-19 Diagnosis. *ACS Cent. Sci.* **2020**, *6*, 591–605.
- (14) Seo, G.; Lee, G.; Kim, M. J.; Baek, S.-H.; Choi, M.; Ku, K. B.; Lee, C.-S.; Jun, S.; Park, D.; Kim, H. G.; Kim, S.-J.; Lee, J.-O.; Kim, B. T.; Park, E. C.; Kim, S. I. Rapid Detection of COVID-19 Causative Virus (SARS-CoV-2) in Human Nasopharyngeal Swab Specimens Using Field-Effect Transistor-Based Biosensor. *ACS Nano* **2020**, *14*, 5135–5142.
- (15) Qiu, G.; Gai, Z.; Tao, Y.; Schmitt, J.; Kullak-Ublick, G. A.; Wang, J. Dual-Functional Plasmonic Photothermal Biosensors for Highly Accurate Severe Acute Respiratory Syndrome Coronavirus 2 Detection. *ACS Nano* **2020**, *14*, 5268–5277.
- (16) Chen, Z.; Zhang, Z.; Zhai, X.; Li, Y.; Lin, L.; Zhao, H.; Bian, L.; Li, P.; Yu, L.; Wu, Y.; Lin, G. Rapid and Sensitive Detection of Anti-SARS-CoV-2 IgG, Using Lanthanide-Doped Nanoparticles-Based Lateral Flow Immunoassay. *Anal. Chem.* **2020**, *92*, 7226–7231.
- (17) He, S.; Liu, K.-K.; Su, S.; Yan, J.; Mao, X.; Wang, D.; He, Y.; Li, L.-J.; Song, S.; Fan, C. Graphene-Based High-Efficiency Surface-Enhanced Raman Scattering-Active Platform for Sensitive and Multiplex DNA Detection. *Anal. Chem.* **2012**, *84*, 4622–4627.
- (18) Kirkcaldy, R. D.; King, B. A.; Brooks, J. T. COVID-19 and Postinfection Immunity: Limited Evidence, Many Remaining Questions. *JAMA* **2020**, *323*, 2245–2246.
- (19) Abbasi, J. The Promise and Peril of Antibody Testing for COVID-19. *JAMA* **2020**, *323*, 1881–1883.
- (20) Long, Q.-X.; Liu, B.-Z.; Deng, H.-J.; Wu, G.-C.; Deng, K.; Chen, Y.-K.; Liao, P.; Qiu, J.-F.; Lin, Y.; Cai, X.-F.; Wang, D.-Q.; Hu, Y.; Ren, J.-H.; Tang, N.; Xu, Y.-Y.; Yu, L.-H.; Mo, Z.; Gong, F.; Zhang, X.-L.; Tian, W.-G.; et al. Antibody Responses to SARS-CoV-2 in Patients with COVID-19. *Nat. Med.* **2020**, *26*, 845–848.
- (21) Wang, L.; Xiong, Q.; Xiao, F.; Duan, H. 2D Nanomaterials Based Electrochemical Biosensors for Cancer Diagnosis. *Biosens. Bioelectron.* **2017**, *89*, 136–151.
- (22) Campuzano, S.; Pedrero, M.; Nikoleli, G. P.; Pingarrón, J. M.; Nikolelis, D. P. Hybrid 2D-Nanomaterials-Based Electrochemical Immunosensing Strategies for Clinical Biomarkers Determination. *Biosens. Bioelectron.* **2017**, *89*, 269–279.

- (23) Zhu, C.; Du, D.; Lin, Y. Graphene-Like 2D nanomaterial-Based Biointerfaces for Biosensing Applications. *Biosens. Bioelectron.* **2017**, *89*, 43–55.
- (24) Stoller, M. D.; Park, S.; Zhu, Y.; An, J.; Ruoff, R. S. Graphene-Based Ultracapacitors. *Nano Lett.* **2008**, *8*, 3498–3502.
- (25) Kim, J.; Ishihara, M.; Koga, Y.; Tsugawa, K.; Hasegawa, M.; Iijima, S. Low-Temperature Synthesis of Large-Area Graphene-Based Transparent Conductive Films Using Surface Wave Plasma Chemical Vapor Deposition. *Appl. Phys. Lett.* **2011**, *98*, 091502.
- (26) Liu, C.; Yu, Z.; Neff, D.; Zhamu, A.; Jang, B. Z. Graphene-Based Supercapacitor with an Ultrahigh Energy Density. *Nano Lett.* **2010**, *10*, 4863–4868.
- (27) Layqah, L. A.; Eissa, S. An Electrochemical Immunosensor for the Corona Virus Associated with the Middle East Respiratory Syndrome Using an Array of Gold Nanoparticle-Modified Carbon Electrodes. *Microchim. Acta* **2019**, *186*, 224.
- (28) Khan, M. S.; Dighe, K.; Wang, Z.; Srivastava, I.; Schwartz-Duval, A. S.; Misra, S. K.; Pan, D. Electrochemical-Digital Immunosensor with Enhanced Sensitivity for Detecting Human Salivary Glucocorticoid Hormone. *Analyst* **2019**, *144*, 1448–1457.
- (29) Khan, M. S.; Misra, S. K.; Dighe, K.; Wang, Z.; Schwartz-Duval, A. S.; Sar, D.; Pan, D. Electrically-Receptive and Thermally-Responsive Paper-Based Sensor Chip for Rapid Detection of Bacterial Cells. *Biosens. Bioelectron.* **2018**, *110*, 132–140.
- (30) Khan, M. S.; Dighe, K.; Wang, Z.; Srivastava, I.; Daza, E.; Schwartz-Duval, A. S.; Ghannam, J.; Misra, S. K.; Pan, D. Detection of Prostate Specific Antigen (PSA) in Human Saliva Using an Ultra-Sensitive Nanocomposite of Graphene Nanoplatelets with Diblock-Co-Polymers and Au Electrodes. *Analyst* **2018**, *143*, 1094–1103.
- (31) Khan, M. S.; Misra, S. K.; Schwartz-Duval, A. S.; Daza, E.; Ostadhossein, F.; Bowman, M.; Jain, A.; Taylor, G.; McDonagh, D.; Labriola, L. T.; Pan, D. Real-Time Monitoring of Post-Surgical and Post-Traumatic Eye Injuries Using Multilayered Electrical Biosensor Chip. *ACS Appl. Mater. Interfaces* **2017**, *9*, 8609–8622.
- (32) Khan, M. S.; Misra, S. K.; Wang, Z.; Daza, E.; Schwartz-Duval, A. S.; Kus, J. M.; Pan, D.; Pan, D. Paper-Based Analytical Biosensor Chip Designed from Graphene-Nanoplatelet-Amphiphilic-Diblock-Co-Polymer Composite for Cortisol Detection in Human Saliva. *Anal. Chem.* **2017**, *89*, 2107–2115.
- (33) Gartia, M. R.; Misra, S. K.; Ye, M.; Schwartz-Duval, A.; Plucinski, L.; Zhou, X.; Kellner, D.; Labriola, L. T.; Pan, D. Point-of-Service, Quantitative Analysis of Ascorbic Acid in Aqueous Humor for Evaluating Anterior Globe Integrity. *Sci. Rep.* **2015**, *5*, 16011.
- (34) Yang, Z.-H.; Zhuo, Y.; Yuan, R.; Chai, Y.-Q. An Amplified Electrochemical Immunosensor Based on *in Situ*-Produced 1-Naphthol as Electroactive Substance and Graphene Oxide and Pt Nanoparticles Functionalized CeO<sub>2</sub> Nanocomposites as Signal Enhancer. *Biosens. Bioelectron.* **2015**, *69*, 321–327.
- (35) von Hauff, E. Impedance Spectroscopy for Emerging Photovoltaics. *J. Phys. Chem. C* **2019**, *123*, 11329–11346.
- (36) Han, J.-H.; Lee, D.; Chew, C. H. C.; Kim, T.; Pak, J. J. A Multi-Virus Detectable Microfluidic Electrochemical Immunosensor for Simultaneous Detection of H1N1, H5N1, and H7N9 Virus Using ZnO Nanorods for Sensitivity Enhancement. *Sens. Actuators, B* **2016**, *228*, 36–42.
- (37) Miodek, A.; Vidic, J.; Sauriat-Dorizon, H.; Richard, C.-A.; Le Goffic, R.; Korri-Youssoufi, H.; Chevalier, C. Electrochemical Detection of the Oligomerization of PB1-F2 Influenza A Virus Protein in Infected Cells. *Anal. Chem.* **2014**, *86*, 9098–9105.
- (38) Huang, J.; Xie, Z.; Xie, Z.; Luo, S.; Xie, L.; Huang, L.; Fan, Q.; Zhang, Y.; Wang, S.; Zeng, T. Silver Nanoparticles Coated Graphene Electrochemical Sensor for the Ultrasensitive Analysis of Avian Influenza Virus H7. *Anal. Chim. Acta* **2016**, *913*, 121–127.
- (39) Wu, Z.; Zhou, C.-H.; Chen, J.-J.; Xiong, C.; Chen, Z.; Pang, D.-W.; Zhang, Z.-L. Bifunctional Magnetic Nanobeads for Sensitive Detection of Avian Influenza A (H7N9) Virus Based on Immunomagnetic Separation and Enzyme-Induced Metallization. *Biosens. Bioelectron.* **2015**, *68*, 586–592.
- (40) Singh, R.; Hong, S.; Jang, J. Label-Free Detection of Influenza Viruses Using a Reduced Graphene Oxide-Based Electrochemical Immunosensor Integrated with a Microfluidic Platform. *Sci. Rep.* **2017**, *7*, 42771.
- (41) Ma, Y.; Shen, X.-L.; Zeng, Q.; Wang, H.-S.; Wang, L.-S. A Multi-Walled Carbon Nanotubes Based Molecularly Imprinted Polymers Electrochemical Sensor for the Sensitive Determination of HIV-p24. *Talanta* **2017**, *164*, 121–127.
- (42) Huang, H.; Bai, W.; Dong, C.; Guo, R.; Liu, Z. An Ultrasensitive Electrochemical DNA Biosensor Based on Graphene/Au Nanorod/Polythionine for Human Papillomavirus DNA Detection. *Biosens. Bioelectron.* **2015**, *68*, 442–446.
- (43) Moitra, P.; Alafeef, M.; Dighe, K.; Frieman, M. B.; Pan, D. Selective Naked-Eye Detection of SARS-CoV-2 Mediated by N Gene Targeted Antisense Oligonucleotide Capped Plasmonic Nanoparticles. *ACS Nano* **2020**, *14*, 7617–7627.
- (44) Alafeef, M.; Srivastava, I.; Pan, D. Machine-Learning for Precision Breast Cancer Diagnosis and Prediction of the Nanoparticles Cellular Internalization. *ACS Sens.* **2020**, *5*, 1689–1698.
- (45) Alafeef, M.; Dighe, K.; Pan, D. Label-Free Pathogen Detection Based on Yttrium-Doped Carbon Nanoparticles up to Single-Cell Resolution. *ACS Appl. Mater. Interfaces* **2019**, *11*, 42943–42955.
- (46) Alafeef, M.; Moitra, P.; Pan, D. Nano-Enabled Sensing Approaches for Pathogenic Bacterial Detection. *Biosens. Bioelectron.* **2020**, *165*, 112276.
- (47) Srivastava, I.; Khan, M. S.; Dighe, K.; Alafeef, M.; Wang, Z.; Banerjee, T.; Ghonge, T.; Grove, L. M.; Bashir, R.; Pan, D. On-Chip Electrical Monitoring of Real-Time “Soft” and “Hard” Protein Corona Formation on Carbon Nanoparticles. *Small Methods* **2020**, *4*, 2000099.
- (48) Vikesland, P. J. Nanosensors for Water Quality Monitoring. *Nat. Nanotechnol.* **2018**, *13*, 651–660.
- (49) Saha, K.; Agasti, S. S.; Kim, C.; Li, X.; Rotello, V. M. Gold Nanoparticles in Chemical and Biological Sensing. *Chem. Rev.* **2012**, *112*, 2739–2779.
- (50) Pingarrón, J. M.; Yáñez-Sedeño, P.; González-Cortés, A. Gold Nanoparticle-Based Electrochemical Biosensors. *Electrochim. Acta* **2008**, *53*, S848–S866.
- (51) Jiang, P.; Wang, Y.; Zhao, L.; Ji, C.; Chen, D.; Nie, L. Applications of Gold Nanoparticles in Non-Optical Biosensors. *Nanomaterials* **2018**, *8*, 977.
- (52) Bastús, N. G.; Comenge, J.; Puntès, V. Kinetically Controlled Seeded Growth Synthesis of Citrate-Stabilized Gold Nanoparticles of Up to 200 nm: Size Focusing versus Ostwald Ripening. *Langmuir* **2011**, *27*, 11098–11105.
- (53) Muntean, C. M.; Dina, N. E.; Coroş, M.; Toşa, N.; Turza, A. I.; Dan, M. Graphene/Silver Nanoparticles-Based Surface-Enhanced Raman Spectroscopy Detection Platforms: Application in the Study of DNA Molecules at Low pH. *J. Raman Spectrosc.* **2019**, *50*, 1849–1860.
- (54) Gupta, A.; Chen, G.; Joshi, P.; Tadigadapa, S.; Eklund, Raman Scattering from High-Frequency Phonons in Supported *n*-Graphene Layer Films. *Nano Lett.* **2006**, *6*, 2667–2673.
- (55) Sheridan, C. Coronavirus and the Race to Distribute Reliable Diagnostics. *Nat. Biotechnol.* **2020**, *38*, 382–384.
- (56) Zhang, X.; Servos, M. R.; Liu, J. Surface Science of DNA Adsorption onto Citrate-Capped Gold Nanoparticles. *Langmuir* **2012**, *28*, 3896–3902.
- (57) Crew, E.; Yan, H.; Lin, L.; Yin, J.; Skeete, Z.; Kotlyar, T.; Tchah, N.; Lee, J.; Bellavia, M.; Goodshaw, I.; Joseph, P.; Luo, J.; Gal, S.; Zhong, C.-J. DNA Assembly and Enzymatic Cutting in Solutions: A Gold Nanoparticle Based SERS Detection Strategy. *Analyst* **2013**, *138*, 4941–4949.
- (58) Ling Ling, T.; Ahmad, M.; Yook Heng, L.; Chee Seng, T. The Effect of Multilayer Gold Nanoparticles on the Electrochemical Response of Ammonium Ion Biosensor Based on Alanine Dehydrogenase Enzyme. *J. Sens.* **2011**, *2011*, 754171.
- (59) Zhang, S.; Wang, N.; Yu, H.; Niu, Y.; Sun, C. Covalent Attachment of Glucose Oxidase to an Au Electrode Modified with



Gold Nanoparticles for Use as Glucose Biosensor. *Bioelectrochemistry* **2005**, 67, 15–22.

(60) Gobbo, P.; Ghiassian, S.; Hesari, M.; Stampelcoskie, K. G.; Kazemi-Zanjani, N.; Lagugné-Labarthe, F.; Workentin, M. S. Electrochemistry of Robust Gold Nanoparticle–Glassy Carbon Hybrids Generated Using a Patternable Photochemical Approach. *J. Mater. Chem.* **2012**, 22, 23971–23980.

(61) Zhao, G.; Liu, G. Electrochemical Deposition of Gold Nanoparticles on Reduced Graphene Oxide by Fast Scan Cyclic Voltammetry for the Sensitive Determination of As(III). *Nanomaterials* **2019**, 9, 41.

(62) Young, S. L.; Kellon, J. E.; Hutchison, J. E. Small Gold Nanoparticles Interfaced to Electrodes through Molecular Linkers: A Platform to Enhance Electron Transfer and Increase Electrochemically Active Surface Area. *J. Am. Chem. Soc.* **2016**, 138, 13975–13984.

(63) Guo, L.; Sun, X.; Wang, X.; Liang, C.; Jiang, H.; Gao, Q.; Dai, M.; Qu, B.; Fang, S.; Mao, Y.; Chen, Y.; Feng, G.; Gu, Q.; Wang, R. R.; Zhou, Q.; Li, W. SARS-CoV-2 Detection with CRISPR Diagnostics. *Cell Discovery* **2020**, 6, 34.

(64) Yu, F.; Yao, D.; Knoll, W. Oligonucleotide Hybridization Studied by a Surface Plasmon Diffraction Sensor (SPDS). *Nucleic Acids Res.* **2004**, 32, No. e75–e75.

(65) Su, Q.; Vogt, S.; Nöll, G. Langmuir Analysis of the Binding Affinity and Kinetics for Surface Tethered Duplex DNA and a Ligand–Apoprotein Complex. *Langmuir* **2018**, 34 (49), 14738–14748.

(66) Xu, S.; Zhan, J.; Man, B.; Jiang, S.; Yue, W.; Gao, S.; Guo, C.; Liu, H.; Li, Z.; Wang, J.; Zhou, Y. Real-Time Reliable Determination of Binding Kinetics of DNA Hybridization Using a Multi-Channel Graphene Biosensor. *Nat. Commun.* **2017**, 8, 14902.

(67) Hurst, S. J.; Lytton-Jean, A. K. R.; Mirkin, C. A. Maximizing DNA Loading on a Range of Gold Nanoparticle Sizes. *Anal. Chem.* **2006**, 78 (24), 8313–8318.

(68) Hadoux, X.; Hui, F.; Lim, J. K. H.; Masters, C. L.; Pébay, A.; Chevalier, S.; Ha, J.; Loi, S.; Fowler, C. J.; Rowe, C.; Villemagne, V. L.; Taylor, E. N.; Fluke, C.; Soucy, J.-P.; Lesage, F.; Sylvestre, J.-P.; Rosa-Neto, P.; Mathotaarachchi, S.; Gauthier, S.; Nasreddine, Z. S.; et al. Non-Invasive *in Vivo* Hyperspectral Imaging of the Retina for Potential Biomarker Use in Alzheimer's Disease. *Nat. Commun.* **2019**, 10, 4227.

(69) Wang, X.; Cui, Y.; Irudayaraj, J. Single-Cell Quantification of Cytosine Modifications by Hyperspectral Dark-Field Imaging. *ACS Nano* **2015**, 9, 11924–11932.

(70) Misra, S. K.; Ostadhossein, F.; Daza, E.; Johnson, E. V.; Pan, D. Hyperspectral Imaging Offers Visual and Quantitative Evidence of Drug Release from Zwitterionic-Phospholipid-Nanocarbon When Concurrently Tracked in 3D Intracellular Space. *Adv. Funct. Mater.* **2016**, 26, 8031–8041.

(71) Schwartz-Duval, A. S.; Misra, S. K.; Mukherjee, P.; Johnson, E.; Acerbo, A. S.; Pan, D. An Anisotropic Propagation Technique for Synthesizing Hyperbranched Polyvillic Gold Nanoparticles. *Nano Res.* **2016**, 9, 2889–2903.

(72) FDA Administration. *In Vitro* Diagnostics EUAs. <https://www.fda.gov/medical-devices/coronavirus-disease-2019-covid-19-emergency-use-authorizations-medical-devices/in-vitro-diagnostics-euas> (accessed July 25, 2020).

(73) Wölfel, R.; Corman, V. M.; Guggemos, W.; Seilmaier, M.; Zange, S.; Müller, M. A.; Niemeyer, D.; Jones, T. C.; Vollmar, P.; Rothe, C.; Hoelscher, M.; Bleicker, T.; Brünink, S.; Schneider, J.; Ehmman, R.; Zwirgmaier, K.; Drosten, C.; Wendtner, C. Virological Assessment of Hospitalized Patients with COVID-2019. *Nature* **2020**, 581, 465–469.

(74) Schedin, F.; Geim, A. K.; Morozov, S. V.; Hill, E. W.; Blake, P.; Katsnelson, M. I.; Novoselov, K. S. Detection of Individual Gas Molecules Adsorbed on Graphene. *Nat. Mater.* **2007**, 6, 652–655.

(75) Ding, Y.; Chan, C. Y.; Lawrence, C. E. S-Fold Web Server for Statistical Folding and Rational Design of Nucleic Acids. *Nucleic Acids Res.* **2004**, 32, W135–W141.

## NOTE ADDED AFTER ASAP PUBLICATION

This article published October 20, 2020 with an incorrect Figure 5 file. The corrected figure published October 21, 2020.